AGU PUBLICATIONS

JGR

Journal of Geophysical Research: Solid Earth

RESEARCH ARTICLE
10.1002/2014JB011678

Key Points:
- AMS in clinopyroxene and orthopyroxene depends on composition and structure
- In augite and diopside, k_1 is tilted 45 degrees from the *c* axis
- AMS degree generally increases with Fe concentration but depends on Fe^{2+}/Fe^{3+}

Supporting Information:
- Text S1
- Tables S1 and S2

Correspondence to:
A. M. Hirt,
ann.hirt@erdw.ethz.ch

Citation:
Biedermann, A. R., T. Pettke, C. Bender Koch, and A. M. Hirt (2015), Magnetic anisotropy in clinopyroxene and orthopyroxene single crystals, *J. Geophys. Res. Solid Earth*, *120*, 1431–1451, doi:10.1002/2014JB011678.

Received 16 OCT 2014
Accepted 25 JAN 2015
Accepted article online 29 JAN 2015
Published online 9 MAR 2015

Magnetic anisotropy in clinopyroxene and orthopyroxene single crystals

Andrea R. Biedermann[1,2], Thomas Pettke[3], Christian Bender Koch[4], and Ann M. Hirt[1]

[1]Institute of Geophysics, ETH Zurich, Zurich, Switzerland, [2]Now at Department of Geology and Mineral Resources Engineering, Norwegian University of Science and Technology, Trondheim, Norway, [3]Institute of Geological Sciences, University of Bern, Bern, Switzerland, [4]Department of Chemistry, University of Copenhagen, Copenhagen, Denmark

Abstract Pyroxenes constitute an important component in mafic igneous and metamorphic rocks. They often possess a prismatic habit, and their long axis, the crystallographic *c* axis, helps define a lineation in a textured rock. Anisotropy of magnetic susceptibility (AMS) serves as a fabric indicator in igneous and metamorphic rocks. If a rock's AMS is carried by pyroxenes, it can be related to their crystallographic preferred orientation and degree of alignment. This requires knowing the intrinsic AMS of pyroxene single crystals. This study provides a comprehensive low-field and high-field AMS investigation of chemically diverse orthopyroxene and clinopyroxene crystals in relation to crystal structure, chemical composition, oxidation state of Fe, and the possible presence of ferromagnetic inclusions. The paramagnetic anisotropy, extracted from high-field data, shows clear relationships to crystallographic directions and Fe concentration both in clinopyroxene and orthopyroxene. In the diopside-augite series, the intermediate susceptibility is parallel to *b*, and the maximum is at 45° to the *c* axis. In aegirine, the intermediate axis remains parallel to *b*, while the maximum susceptibility is parallel to *c*. The AMS of spodumene depends on Fe concentration. In enstatite, the maximum susceptibility aligns with *c* and the minimum with *b*, and in the case of hypersthene, the maximum susceptibility is normal to the exsolution lamellae. Magnetite inclusions within augite possess a ferromagnetic anisotropy with consistent orientation of the principal susceptibilities, which dominates the low-field anisotropy. These results provide better understanding of magnetic anisotropy in pyroxenes and form a solid basis for interpretation of magnetic fabrics in pyroxene-bearing rocks.

1. Introduction

Pyroxenes are common minerals in mafic and ultramafic igneous and metamorphic rocks. Orthopyroxene in particular is an important constituent of the Earth's upper mantle [*Deer et al.*, 1978]. Pyroxenes are single-chain silicates in which $(Si_2O_6^{4-})_n$ chains are linked by cations (Figure 1). The cations can occupy two nonequivalent sites, M1 and M2. In clinopyroxenes, the M2 site is strongly distorted with an irregular sixfold (spodumene) or eightfold (augite, diopside, and aegirine) coordination and generally occupied by Ca, Na, K, or Li. The M1 site is coordinated by a nearly regular octahedron and generally occupied by the smaller cations Mg, Fe^{2+}, Fe^{3+}, Mn, Al, or Ti. Fe^{2+} is normally located in the M1 site, but if not enough Ca (or other large cations) is present to fully occupy M2, Fe^{2+} prefers M2 sites. Clinopyroxene is monoclinic with space group *C*2/*c*. Orthopyroxenes contain no significant amounts of Ca, and due to the overall smaller radius of the cations in the M1 and M2 sites, their crystal structure is orthorhombic (space group *Pbca*). Similar to clinopyroxenes, orthopyroxenes possess M1 and M2 sites, where the M1 site is coordinated in an almost regular octahedron and the M2 sites have a distorted sixfold coordination. Fe^{2+} prefers the M2 sites in orthopyroxenes [*Deer et al.*, 1978]. The structure of both pyroxene groups consists of long covalently bonded chains in the *c* direction, which are linked by weaker ionic bonds in directions perpendicular to the chains; consequently, clinopyroxenes and orthopyroxenes have well-defined cleavage on {110} and {210}, respectively [*Deer et al.*, 1978]. Therefore, pyroxenes often display prismatic habits, and their *c* axis aligns with the rock lineation, thus indicating flow directions or deformation in igneous and metamorphic rocks, respectively.

Anisotropy of magnetic susceptibility (AMS) is often used as a proxy for rock texture [e.g., *Borradaile and Henry*, 1997; *Hrouda*, 1982, and references therein]. Magnetic susceptibility is a second-order tensor property, represented by a symmetric 3×3 matrix whose eigenvalues correspond to the principal susceptibilities $k_1 \geq k_2 \geq k_3$, and the respective eigenvectors reflect their directions. Magnetic anisotropy can be carried by ferromagnetic grains or by Fe-bearing silicates, e.g., pyroxene, with crystallographic preferred orientation. For example, the

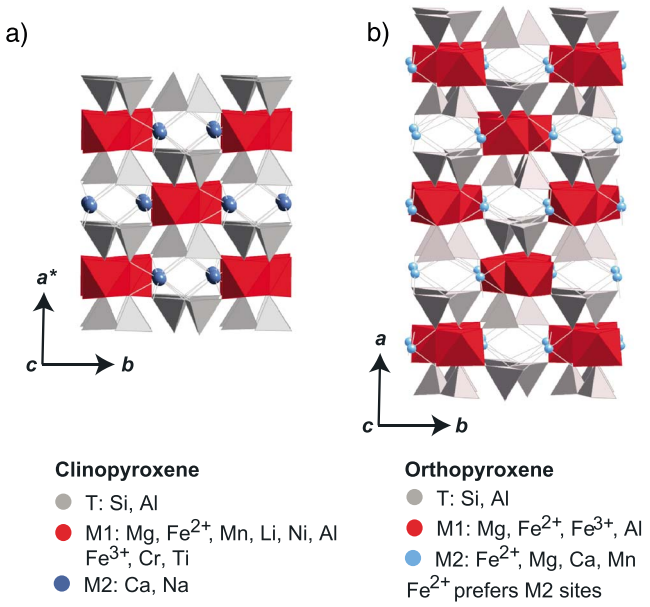

Figure 1. Crystal structure and typical site occupancies for (a) clinopyroxene and (b) orthopyroxene. Figure generated with CrystalMaker.

AMS of an aegirine-augite syenite from the Triunfo pluton in Brazil is controlled by aegirine-augite [*Archanjo and Bouchez*, 1997]. The authors found an oblate magnetic fabric and suggested that this may be caused by (1) an oblate single-crystal AMS of the clinopyroxene or (2) the compaction of the magma chamber after emplacement. A conclusive interpretation of the magnetic fabric was not possible, because the single-crystal properties of clinopyroxenes are not well established. This and a recent study by *Selkin et al.* [2014] illustrate that a good quantitative understanding of single-crystal magnetic properties is essential before using the magnetic fabric as a strain indicator.

At present, there are only a few studies on the intrinsic magnetic anisotropy of clinopyroxene and orthopyroxene crystals. Some of these indicate that the maximum susceptibility in pyroxene is not always parallel to the crystallographic *c* axis. In the early twentieth century, *Finke* [1909] measured one augite crystal and found that k_1 is at a −7° angle to the *c* axis. Later, *Parry* [1971] (cited in *Wagner et al.* [1981]) measured 19 augite crystals using high-field torque magnetometry and concluded that the intermediate susceptibility k_2 is always parallel to *b* and k_1 and k_3 lie in between the *c* and ±*a* axes. *Lagroix and Borradaile* [2000] measured four clinopyroxenes, with a special focus on the ferromagnetic inclusions within the pyroxenes, and found that in three crystals the intermediate susceptibility is parallel to *b*, whereas no symmetry was found for k_1 or k_3. Two studies exist on orthopyroxenes; *Wiedenmann et al.* [1986] studied synthetic and natural Fe-rich orthopyroxene and found that k_1 is parallel to *b* and antiferromagnetic ordering sets in at sufficiently low temperatures. *Lagroix and Borradaile* [2000] measured five orthopyroxene samples and found that the maximum susceptibility is parallel to *c*. They did not find any relationship between k_2 and k_3 to either *a* or *b* and attributed this to ferromagnetic inclusions or misorientation.

These few investigations show no consistent relationship between the principal susceptibility axes and the crystallographic axes. Studies on other mineral groups have shown the influence of chemical composition on the degree of AMS and orientation of principal axes [*Almqvist et al.*, 2010; *Biedermann et al.*, 2014b; *Schmidt et al.*, 2007a]. The exact chemical composition of the crystals was only given in one study on orthopyroxene [*Wiedenmann et al.*, 1986]; therefore, little information is available on the effects of chemical composition, or site distribution and oxidation state of Fe, which may vary considerably, on the magnetic properties.

In this study, a systematic investigation of magnetic anisotropy in clinopyroxene and orthopyroxene of various compositions is conducted. Bulk chemistry, oxidation states of Fe, and site distributions are determined in order to gain a complete understanding of factors that influence the degree of paramagnetic anisotropy and the orientation of the principal axes with respect to the crystallographic axes.

2. Material and Methods

2.1. Samples and Sample Preparation

Samples were collected to cover a wide range of chemical compositions and include crystals from the mineral groups diopside, augite, aegirine, spodumene, and enstatite. Good quality single crystals were obtained from different sources; (1) the Natural History Museum Basel (labeled NMB), (2) the ETH Mineral Collection, (3) mineral suppliers, and (4) field work in Tenerife and on Isola Vulcano. In addition, two hypersthene samples, consisting of lamellar intergrowth of clinopyroxene and orthopyroxene, were measured. An overview of samples and their localities is given in Table 1.

Table 1. List of Samples With Their Geologic Locality

	Sample	Mineral	Mass (g)	Locality	Comment
				Clinopyroxenes	
Calcium pyroxenes					
Diopside					
	Di1	diopside	2.66	unknown	
	Di2	diopside	1.69	Merelani, Arusha, Tanzania	
	Di3	diopside	4.51	Tormiq, Baltistan, Pakistan	
	Di4	diopside	3.79	Tormiq, Baltistan, Pakistan	
	Di5	diopside	7.33	Cranberry Lake, Battersea, Ontario, Canada	
	Di6	diopside	2.15	unknown	
	Di7	diopside	2.63	unknown	
	NMB15591	diopside	1.96	Val di Fassa, Prov. Trento, Trentino-Alto Adige, Italy	
	NMB346	diopside	0.96	Ala, Prov. Trento, Trentino-Alto Adige, Italy	
	NMB5681	diopside	7.96	Papineauville, Québec, Canada	
Augite					
	Aug1	augite	0.99	unknown	
	NMB42516	augite	0.57	Preduzzo, Prov. Trento, Trentino-Alto Adige, Italy	
	NMB46281	augite	5.38	Monte Caro, Lago Albani, Prov. Rome, Lazio, Italy	
	T1	augite	0.71	Tenerife, Canary Islands, Spain	
	T2	augite	1.38	Tenerife, Canary Islands, Spain	twinned
	T3	augite	0.52	Tenerife, Canary Islands, Spain	
	T4	augite	0.59	Tenerife, Canary Islands, Spain	
	T5	augite	0.74	Tenerife, Canary Islands, Spain	
	T6	augite	0.55	Tenerife, Canary Islands, Spain	
	T7	augite	0.71	Tenerife, Canary Islands, Spain	
	T8	augite	0.74	Tenerife, Canary Islands, Spain	
	T9	augite	0.37	Tenerife, Canary Islands, Spain	
	T10	augite	0.28	Tenerife, Canary Islands, Spain	
	T12	augite	0.95	Tenerife, Canary Islands, Spain	
	T13	augite	0.40	Tenerife, Canary Islands, Spain	
	T14	augite	0.37	Tenerife, Canary Islands, Spain	
	T15	augite	0.78	Tenerife, Canary Islands, Spain	
	T16	augite	0.43	Tenerife, Canary Islands, Spain	
	T17	augite	0.42	Tenerife, Canary Islands, Spain	
	T18	augite	0.20	Tenerife, Canary Islands, Spain	
	T19	augite	0.81	Tenerife, Canary Islands, Spain	
	Vul1	augite	0.83	Isola Vulcano, Italy	
	Vul2	augite	0.30	Isola Vulcano, Italy	
	Vul3	augite	0.22	Isola Vulcano, Italy	
	Vul4	augite	0.10	Isola Vulcano, Italy	twinned
	Vul5	augite	0.12	Isola Vulcano, Italy	twinned
	Vul6	augite	0.07	Isola Vulcano, Italy	twinned
	Vul7	augite	0.12	Isola Vulcano, Italy	twinned
	A4	augite	3.36	Lodmurwak Maar, Tanzania	
	A6	augite	0.49	Lodmurwak Maar, Tanzania	
Sodium pyroxenes					
Aegirine					
	Aeg1	aegirine	6.89	Mt. Malosa, Zomba District, Malawi	
	Aeg2	aegirine	5.99	Mt. Malosa, Zomba District, Malawi	
	Aeg3	aegirine	6.25	Mt. Malosa, Zomba District, Malawi	
	Aeg4	aegirine	5.76	Mt. Malosa, Zomba District, Malawi	
	Aeg5	aegirine	4.68	Mt. Malosa, Zomba District, Malawi	
	Aeg6	aegirine	0.33	Mt. Malosa, Zomba District, Malawi	two individuals with slightly different orientation
	Aeg7	aegirine	0.29	Mt. Malosa, Zomba District, Malawi	two individuals with slightly different orientation
	Aeg8	aegirine	0.28	Mt. Malosa, Zomba District, Malawi	two individuals with slightly different orientation
	Aeg9	aegirine	0.31	Mt. Malosa, Zomba District, Malawi	twinned

Table 1. (continued)

	Sample	Mineral	Mass (g)	Locality	Comment
	Aeg10	aegirine	0.24	Mt. Malosa, Zomba District, Malawi	
	Aeg11	aegirine	0.10	Mt. Malosa, Zomba District, Malawi	
Lithium pyroxenes					
Spodumene					
	NMB444	spodumene	0.69	Stony Point, Alexander County, North Carolina, USA	
	Spod1	spodumene (kunzite)	2.40	Minas Gerais, Brazil	
	Spod2	spodumene (kunzite)	2.74	Minas Gerais, Brazil	
	Spod3	spodumene (hiddenite)	1.55	Minas Gerais, Brazil	
	Spod4	spodumene (hiddenite)	1.49	Minas Gerais, Brazil	
	fXl	spodumene (colorless)	1.14	unknown	
	fXl2	spodumene (colorless)	1.30	unknown	
				Orthopyroxenes	
Mg-Fe pyroxenes					
Enstatite					
	En1	enstatite	3.72	Kilosa, Morogoro, Tanzania	
	En2	enstatite	3.03	Kilosa, Morogoro, Tanzania	
	En3	enstatite	2.74	Kilosa, Morogoro, Tanzania	
	NMB45706	enstatite	1.09	Salem, India	
Hypersthene					
	Hyp1	hypersthene	2.68	Canada	exsolution lamellae of cpx
	Hyp2	hypersthene	2.88	Canada	exsolution lamellae of cpx

If needed, samples were first separated from the host rock. They were cleaned in ethanol in an ultrasonic cleaner and weighed. Crystal orientation was determined based on the crystal habit and Laue X-ray diffraction, which was performed at the Laboratory of Crystallography, ETH Zurich. Laue images were processed with the OrientExpress 3.4 crystal orientation software [*Laugier and Filhol*, 1983]. Based on Laue images obtained from different crystal faces, it was possible to identify twinning on {100} in some of the augite crystals and one aegirine crystal. Three of the aegirine samples showed a superposition of two Laue patterns corresponding to two individual crystals with slightly different orientation. Because both features are common in clinopyroxene, these samples were also included in the study (cf. Table 1). The oriented samples were glued into cylindrical plastic holders for the magnetic measurements. Surfaces were polished prior to chemical analysis if required.

2.2. Chemistry

2.2.1. Bulk Chemistry

Bulk chemical composition was determined using laser ablation inductively coupled plasma mass spectroscopy (LA-ICP-MS) at the Institute of Geological Sciences, University of Bern. LA-ICP-MS was preferred over electron probe microanalysis because LA-ICP-MS analyzes a sample volume per spot that is several orders of magnitude larger than that for microprobe analyses. This means that possible inclusion materials (minerals or melt inclusions) are included in the analyses. LA-ICP-MS has an additional advantage that entire crystals or large pieces thereof can be analyzed without the need for perfectly polished sections. Four to six spots were measured on crystal surfaces, polished crystal surfaces, or/and cleavage planes for each sample. Measurements were performed with a beam diameter of 90 or 120 μm, after the surface had been cleaned with a larger beam. SRM610 and SRM612 from the National Institute of Standards and Technology were used for external standardization, with values reported in *Spandler et al*. [2011]. The measurement procedure and settings are described in *Pettke et al*. [2012]. The data were processed using SILLS [*Guillong et al*., 2008], normalized to 100 wt % total major oxides and averaged for further investigation. Note that additional information is needed in order to determine the oxidation state of Fe. Therefore, the total Fe concentration was determined assuming that all Fe is present as Fe^{2+} in diopside, augite, spodumene, and the orthopyroxenes. For aegirine, it was assumed that all Fe is Fe^{3+}, according to the ideal chemical composition.

2.2.2. Mössbauer Spectra

In order to determine the relative proportion of Fe^{2+} and Fe^{3+} in the crystals and investigate details in the coordination sites, Mössbauer spectra were measured on selected clinopyroxene samples. Absorbers were prepared by mixing powdered mineral samples and BN and transferring the mix into Perspex^R sample holders.

Spectra were obtained at room temperature using a conventional constant acceleration spectrometer with the absorber perpendicular to the gamma ray direction. The spectrometer was calibrated using the spectrum of a thin foil of natural iron at room temperature, and isomer shifts are given relative to the center of this absorber. The spectra were fitted using a combination of doublet components having Lorentzian line shape, and it was assumed that relative spectral areas are identical to relative abundances of the components.

2.2.3. Recalculation of Mineral Formulae

Mineral formulae were recalculated based on the assumption that four cations (including Si) are present per formula unit. The cations were then assigned to the tetrahedral sites within the chains, where Al can substitute for Si, and the M1 and M2 sites. Where Mössbauer data were available, the Fe^{3+} concentration was determined based on these. In order to test the analyses, the total positive charge, which should amount to 12, was calculated.

2.3. Magnetic Measurements

2.3.1. Characterization of Ferromagnetic Inclusions

Many minerals, even single crystals, contain inclusions of other phases. For magnetic studies, ferromagnetic inclusions such as magnetite are of major interest, because they possess a large susceptibility. Hence, even small fractions of such inclusions strongly influence the bulk magnetic properties of the sample. Acquisition of isothermal remanent magnetization (IRM) was measured in order to verify the presence of ferromagnetic inclusions. The magnitude of the saturation IRM provides an estimate of the concentration of ferromagnetic material in the sample. The crystals were magnetized first along the $-c$ direction in a 2 T field using an ASC Scientific IM-10-30 Pulse Magnetizer. Subsequently, the crystal was remagnetized along the $+c$ direction in increasing fields between 20 mT and 2 T. The magnetization was measured on a 2G Enterprises, three-axis, cryogenic magnetometer (Model 755) after each step.

2.3.2. Magnetic Susceptibility and Anisotropy of Magnetic Susceptibility

Low-field susceptibility was measured on an AGICO MFK1-FA susceptibility bridge, in fields of 200 A/m or 500 A/m and a frequency of 976 Hz. Magnetic susceptibility was measured in 15 directions. Directional susceptibility measurements were repeated 10 times for each position and averaged, in order to receive the best possible signal quality [*Biedermann et al*., 2013]. The full magnetic susceptibility tensor was computed from these directional measurements. Mean susceptibility (k_{mean}) is calculated as the arithmetic mean of the three eigenvalues of this tensor. The degree of the anisotropy will be described by $k' = \sqrt{\left[(k_1 - k_{mean})^2 + (k_2 - k_{mean})^2 + (k_3 - k_{mean})^2\right]/3}$ and $P = k_1/k_3$ and the shape of the AMS ellipsoid by $U = (2k_2 - k_1 - k_3)/(k_1 - k_3)$ [*Jelinek*, 1981, 1984]. Even small amounts of ferromagnetic inclusions can dominate the low-field AMS. For this reason, high-field AMS was measured in addition to low-field AMS. High-field methods make it possible to isolate the component of the AMS carried by paramagnetic minerals alone. The high-field measurements were performed on a torque magnetometer, in various fields between 1.0 T and 1.5 T [*Bergmüller et al*., 1994]. In such high fields, the ferromagnetic magnetization is saturated, while the paramagnetic magnetization increases with the applied field. The different field dependence allows for separation of the ferromagnetic and the paramagnetic components, whose relative contributions and uncertainties can be estimated based on the method described by *Martín-Hernández and Hirt* [2001]. High-field AMS was determined both at room temperature (RT) and at 77 K and is described by k' and U like the low-field AMS. At low temperature, the paramagnetic signal is enhanced [*Schmidt et al*., 2007b]. This enhancement can be quantified by $p'_{77} = \frac{k'(77K)}{k'(RT)}$.

3. Results

3.1. Chemistry

Average chemical compositions are summarized in Table S1 in the supporting information. Whereas some samples show zonation, most are homogeneous on a crystal scale. The only exception is hypersthene (samples Hyp1 and Hyp2), which consists of Ca-rich clinopyroxene exsolution lamellae and Ca-poor orthopyroxene. For these samples, the composition given in Table S1 is the average of all measurements, hence represents the average high-temperature composition prior to exsolution. One augite, NMB46281, was too large to fit the ablation chamber and could thus not be analyzed by LA-ICP-MS. The samples cover a wide range of Fe concentrations, which lie between 0.005 and 29.6 wt % FeO in the clinopyroxene and between 0.6 and 15.3 wt % FeO in the orthopyroxene group. Other elements with strong magnetic moments

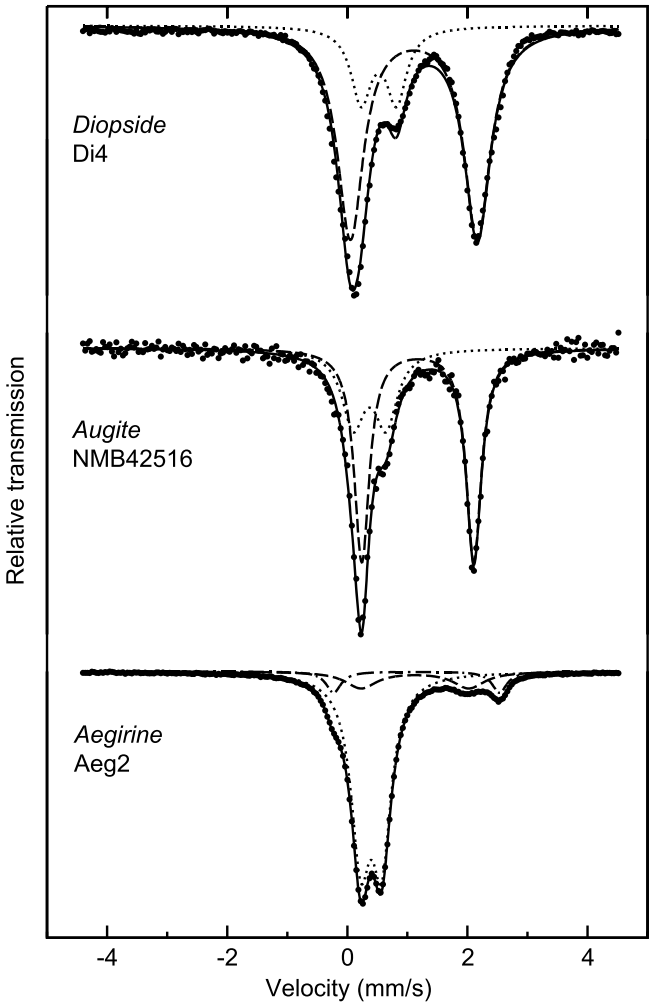

Figure 2. Characteristic Mössbauer spectra for selected samples.

were only present in small amounts: MnO < 0.7 and 0.3 wt %, Cr < 4050 and < 3000 μg/g, and Ni < 2020 and < 1450 μg/g in clinopyroxene and orthopyroxene, respectively.

Representative Mössbauer spectra and fits are shown in Figure 2, and hyperfine parameters are given in Table 2. The spectra exhibit different characteristics for diopside, augite, and aegirine. The diopside samples exhibit one dominant doublet (one high spin Fe^{2+}) and one unresolved Fe^{3+} doublet overlapping the low velocity line of the Fe^{2+} doublet, which yields 66% Fe^{2+} and 34% Fe^{3+} in the two samples. The augite samples exhibit three absorption peaks that are interpreted to be an overlap of two doublet components (one high spin Fe^{2+} and one high spin Fe^{3+}) resulting in Fe^{2+} areas between approximately 60 and 80% and Fe^{3+} areas between approximately 40 and 20%. The aegerine samples exhibit one dominant doublet of high spin Fe^{3+}, one minor, partially resolved Fe^{2+}, and one minor, unresolved Fe^{2+} resulting in 80 to 87% Fe^{3+} and 13 to 21% Fe^{2+} in two sites. Different interpretations have been proposed for the varying doublets in clinopyroxenes [e.g., *Abdu and Hawthorne*, 2013; *Redhammer et al*., 2006], but because the main interest in this study lies on the relative proportions of Fe^{2+} and Fe^{3+}, they will not be discussed further.

Recalculated site occupancies are shown in Table S2 (supporting information). The M2 sites of diopside and augite are mainly filled with Ca; however, not all samples contain enough Ca to occupy all M2 sites. Fe^{2+} preferentially fills this Ca vacancy, but, in general, the Fe^{2+} concentration is higher in M1 than in M2 [*Burns*, 1993]. Therefore, and in accordance with *Deer et al*. [1978], all Fe^{2+} is assigned to the M1 sites. The dominant cation in the M1 sites is Mg for diopside and various combinations of Mg, Al, and Fe^{2+} in the augite samples. In aegirine, Na replaces Ca in the M2 sites, and the M1 sites contain mainly Fe. In the ideal formula, the latter is present as Fe^{3+}, which is confirmed by Mössbauer data on selected crystals. The M1 sites in spodumene are filled mainly by Al and the M2 sites by Li. For enstatite, only very small amounts of Ca are present and both M1 and M2 sites are occupied by Mg or Fe. In this configuration, Fe^{2+} prefers M2 sites, whereas Fe^{3+} and Al are preferentially located in M1 [*Deer et al*., 1978]. The site occupancies shown for hypersthene correspond to the homogeneous high-temperature orthopyroxene prior to exsolution.

3.2. Mass Susceptibility

Mean mass susceptibility in clinopyroxene ranges from -5.86×10^{-9} m^3/kg to 6.98×10^{-6} m^3/kg for diopside, -3.78×10^{-8} m^3/kg to 1.00×10^{-8} m^3/kg for spodumene, and 5.68×10^{-7} m^3/kg to 6.73×10^{-7} m^3/kg for aegirine and covers a wide range from 1.57×10^{-7} m^3/kg to 2.73×10^{-5} m^3/kg in augite. One diopside and six spodumene crystals are diamagnetic. The mean susceptibility lies between 7.00×10^{-9} m^3/kg and 1.08×10^{-6} m^3/kg for

Table 2. Hyperfine Parameters and Relative Areas of Fe^{2+} and Fe^{3+} Components as Derived From Mössbauer Spectroscopy

		Component 1: Fe^{3+}				Component 2: Fe^{2+}				Component 3: Fe^{2+}				
Sample	Comment	Isomer Shift (mm/s)	Quadrupole Splitting (mm/s)	Line Width (mm/s)	Area %	Isomer Shift (mm/s)	Quadrupole Splitting (mm/s)	Line Width (mm/s)	Area %	Isomer Shift (mm/s)	Quadrupole Splitting (mm/s)	Line Width (mm/s)	Area %	Fe^{2+}/Fe^{3+}
						Diopside								
Di3		0.36	0.60	0.77	34	1.19	1.88	0.32	66					1.95
Di4		0.37	0.55	0.47	34	1.17	1.87	0.30	66					1.93
						Augite								
NMB42516		0.53	0.59	0.40	21	1.11	2.11	0.53	79					3.71
T3	with magnetite	0.53	0.65	0.56	43	1.05	2.20	0.61	57					1.33
T7		0.51	0.64	0.54	38	1.05	2.22	0.61	62					1.60
T18		0.52	0.66	0.56	42	1.05	2.23	0.58	58					1.36
Vul2		0.55	0.59	0.40	23	1.13	2.12	0.52	77					3.34
						Aegirine								
Aeg2		0.40	0.35	0.39	80	1.13	1.79	0.63	13	1.15	2.76	0.30	8	0.25
Aeg5		0.39	0.33	0.33	87	1.11	1.76	0.32	6	1.15	2.74	0.33	7	0.15

orthopyroxene (Table 3). According to *Vernon* [1961] and *Bleil and Petersen* [1982], the susceptibility of a paramagnetic material can be calculated based on the concentration of strongly magnetic ions such as Fe or Mn. In the crystal collection in this study, the concentrations of Mn or other cations with strong magnetic moments are low (Table S1); thus, the paramagnetic susceptibility can be estimated based on Fe concentration alone. For clinopyroxene, the effective magnetic moment of Fe^{2+} is $6.06\mu_B$ and for orthopyroxene it is $5.08\mu_B$ [*Parks and Akhtar*, 1968]. No experimental values are available for the effective magnetic moment of Fe^{3+} in pyroxenes, and therefore, the theoretical value of $5.88\mu_B$ is used [*Parks and Akhtar*, 1968; *Vernon*, 1961]. Thus, the theoretical paramagnetic susceptibility can be computed as $\chi = 2.70 \times 10^{-8} \times Fe\,\mathrm{m}^3/\mathrm{kg}$ for diopside, augite, and spodumene, $2.54 \times 10^{-8} \times Fe\,\mathrm{m}^3/\mathrm{kg}$ for aegirine, and $1.89 \times 10^{-8} \times Fe\,\mathrm{m}^3/\mathrm{kg}$ for orthopyroxene, where *Fe* is the Fe concentration in weight percent. A good agreement between calculated and measured susceptibilities was found for diopside and enstatite (Table 3 and Figure 3). The calculation does not take into account the diamagnetic component, and therefore, the theoretical susceptibility for spodumene is larger than that measured. For aegirine, the calculated susceptibility is generally lower than the measured one. This might be related to the fact that the effective magnetic moment is not well defined for Fe^{3+} in clinopyroxene, in general, and specifically in aegirine. Experimental data would be needed, as the effective magnetic moment of Fe^{3+} in compounds can vary, depending on the crystal field, as has been shown by a study on ferric complex ions by *Werbel et al.* [1943]. All augite crystals and one diopside have significantly larger susceptibilities than expected; these can be attributed to ferromagnetic inclusions in the crystals (Figure 3a, inset).

3.3. Identification of Ferromagnetic Inclusions

IRM increases rapidly in low fields, and remanent coercivity is low for all crystals except Aeg3, whose remanent coercivity is 185 mT. The augite and hypersthene samples show the highest IRM and exhibit remanent coercivities < 20 mT. This is indicative of a low coercivity phase, typically magnetite or maghemite. The ferromagnetic inclusions in Di5, Spod1, Aeg6, and En1 have higher

Journal of Geophysical Research: Solid Earth

10.1002/2014JB011678

Table 3. Measured and Calculated Mass Susceptibility, and Principal Susceptibilities and Directions of the Low-Field AMS With Anisotropy Degree, Shape and Significance

		Mass Susceptibility	Theoretical Susceptibility													
	Sample	(m^3/kg)	(m^3/kg)	k_1	D (deg)	I (deg)	k_2	D (deg)	I (deg)	k_3	D (deg)	I (deg)	k' (m^3/kg)	P	U	R_1
							Clinopyroxenes									
Calcium pyroxenes																
Diopside																
	Di1	6.63E−08	5.52E−08	1.054	206.2	34.2	1.047	107.0	13.2	0.899	359.1	52.7	4.75E−09	1.17	0.90	21.0
	Di2	−5.86E−09	7.39E−10	1.063	358.2	9.4	0.997	259.6	42.2	0.940	98.2	46.3	2.94E−10	1.13	−0.07	0.8
	Di3	2.63E−08	3.55E−08	1.039	194.3	47.2	1.022	99.3	4.6	0.939	5.1	42.4	1.14E−09	1.11	0.65	4.2
	Di4	5.32E−08	4.90E−08	1.047	178.9	45.5	1.016	270.3	1.4	0.938	1.6	44.5	2.44E−09	1.12	0.42	7.5
	Di5	1.88E−08	2.99E−08	1.091	171.9	53.3	1.012	264.9	2.2	0.897	356.6	36.6	1.51E−09	1.22	0.19	10.6
	Di6	1.25E−08	2.08E−08	1.103	176.8	40.8	1.028	81.6	6.0	0.869	344.8	48.5	1.22E−09	1.27	0.36	2.2
	Di7	1.32E−08	2.29E−08	1.071	155.8	64.0	1.009	275.3	13.5	0.920	10.8	21.8	8.23E−10	1.16	0.18	1.8
	NMB15591	1.40E−08	2.73E−08	1.179	179.3	36.7	1.035	89.1	0.3	0.787	358.7	53.3	2.26E−09	1.50	0.27	3.4
	NMB346	9.01E−09	2.80E−08	1.269	168.8	52.1	0.996	264.1	4.1	0.735	357.3	37.6	1.96E−09	1.73	−0.02	2.0
	NMB5681	6.98E−06	1.52E−08	1.104	174.8	4.9	1.025	265.0	2.3	0.871	19.9	84.6	6.74E−07	1.27	0.33	8.4
Augite																
	Aug1	3.42E−06	1.86E−07	1.013	262.6	9.0	1.001	163.5	45.1	0.986	1.3	43.5	3.70E−08	1.03	0.16	6.7
	NMB42516	4.77E−06	2.62E−07	1.034	152.6	60.0	0.988	278.8	18.8	0.978	16.9	22.5	1.17E−07	1.06	−0.63	6.8
	NMB46281	1.57E−07		1.033	182.0	49.4	1.013	279.3	6.2	0.954	14.5	39.9	5.27E−09	1.08	0.50	24.2
	T1	1.09E−05	1.75E−07	1.017	13.1	49.3	1.006	185.2	40.4	0.977	278.6	3.9	1.84E−07	1.04	0.44	22.6
	T2	1.10E−05	2.22E−07	1.058			1.007			0.935			5.54E−07	1.13	0.17	21.4
	T3	1.28E−05	1.66E−07	1.017	160.5	67.4	1.008	344.0	22.6	0.975	253.5	1.2	2.32E−07	1.04	0.57	20.9
	T4	1.18E−05	1.92E−07	1.048	304.5	54.0	1.017	193.6	14.5	0.935	94.3	32.1	5.56E−07	1.12	0.46	71.3
	T5	1.53E−05	1.77E−07	1.076	7.2	6.3	0.984	274.9	19.7	0.940	114.1	69.2	8.69E−07	1.14	−0.35	65.3
	T6	1.05E−05	1.69E−07	1.042	111.8	25.5	1.028	16.4	11.2	0.931	264.8	61.8	5.17E−07	1.12	0.75	52.3
	T7	2.55E−05	1.67E−07	1.257	199.1	80.5	0.920	57.2	7.5	0.822	326.4	5.8	4.75E−06	1.53	−0.55	467.4
	T8	8.93E−06	1.79E−07	1.073	235.8	69.3	1.058	347.4	7.9	0.869	80.2	19.0	8.32E−07	1.24	0.85	65.5
	T9	1.85E−05	1.73E−07	1.152	179.3	38.9	1.030	15.2	50.0	0.818	275.7	7.9	2.55E−06	1.41	0.27	154.5
	T10	6.82E−06	1.74E−07	1.213	6.0	64.2	1.073	175.7	25.5	0.713	267.7	4.0	1.44E−06	1.70	0.44	99.1
	T12	1.60E−05	1.90E−07	1.055	149.6	75.1	1.032	6.3	12.0	0.913	274.4	8.6	9.96E−07	1.16	0.68	89.8
	T13	1.88E−05	1.71E−07	1.156	183.1	17.3	1.083	335.7	70.6	0.761	90.5	8.4	3.23E−06	1.52	0.63	93.5
	T14	8.72E−06	1.75E−07	1.229	193.0	41.6	1.039	0.7	47.7	0.733	97.5	6.1	1.78E−06	1.68	0.23	115.7
	T15	2.73E−05	1.61E−07	1.095	157.9	40.0	1.001	267.2	21.5	0.904	18.2	42.3	2.12E−06	1.21	0.02	214.9
	T16	1.02E−05	1.69E−07	1.193	181.7	17.4	1.110	3.8	72.6	0.697	271.9	0.6	2.22E−06	1.71	0.66	127.4
	T17	1.59E−05	1.73E−07	1.106	196.9	20.0	1.013	41.7	68.2	0.881	290.0	8.4	1.47E−06	1.26	0.17	96.0
	T18	1.43E−05	1.68E−07	1.174	140.6	59.0	1.027	356.7	25.9	0.798	258.8	15.8	2.21E−06	1.47	0.22	70.8
	T19	1.82E−05	1.84E−07	1.173	182.9	58.8	1.089	3.2	31.2	0.738	273.2	0.1	3.42E−06	1.59	0.62	228.8
	Vul1	4.63E−06	2.45E−07	1.027	153.5	7.5	1.010	25.0	78.1	0.964	244.8	9.2	1.23E−07	1.07	0.46	18.6
	Vul2	2.78E−06	2.42E−07	1.085	192.5	64.7	1.038	355.9	24.4	0.878	88.8	6.4	2.47E−07	1.24	0.54	52.1
	Vul3	2.78E−06	2.47E−07	1.111	178.2	25.8	1.018	5.0	64.0	0.871	269.5	2.7	2.75E−07	1.28	0.22	48.1
	Vul4	1.38E−06	2.48E−07	1.052			0.993			0.955			5.48E−08	1.10	−0.22	7.6
	Vul5	8.11E−06	2.52E−07	1.036			1.019			0.945			3.21E−07	1.10	0.64	26.5
	Vul6	3.53E−06	2.58E−07	1.134			1.049			0.818			4.72E−07	1.39	0.46	13.2
	Vul7	3.93E−06	2.53E−07	1.101			1.095			0.804			5.46E−07	1.37	0.96	55.1
	A4	1.25E−06	1.28E−07	1.050	7.2	16.2	1.032	157.3	71.4	0.918	274.6	8.8	7.28E−08	1.14	0.72	44.7
	A6	4.63E−07	1.23E−07	1.152	190.1	28.0	1.014	337.1	57.7	0.834	92.0	14.9	6.02E−08	1.38	0.14	44.3

Journal of Geophysical Research: Solid Earth

10.1002/2014JB011678

Table 3. (continued)

	Sample	Mass Susceptibility (m^3/kg)	Theoretical Susceptibility (m^3/kg)	k_1	D (deg)	I (deg)	k_2	D (deg)	I (deg)	k_3	D (deg)	I (deg)	k' (m^3/kg)	P	U	R_1
Sodium pyroxenes																
Aegirine																
	Aeg1	6.73E−07	7.04E−07	1.003	294.9	83.7	1.000	76.3	4.9	0.997	166.6	3.9	1.66E−09	1.01	−0.20	3.4
	Aeg2	6.61E−07	7.18E−07	1.004	275.3	81.7	0.999	87.2	8.3	0.996	177.4	1.2	2.21E−09	1.01	−0.26	1.6
	Aeg3	6.53E−07	7.32E−07	1.006	262.7	82.2	0.999	86.6	7.8	0.995	356.5	0.5	2.89E−09	1.01	−0.17	2.8
	Aeg4	6.57E−07	7.12E−07	1.003	248.2	76.0	1.000	64.1	14.0	0.997	154.3	1.0	1.77E−09	1.01	0.00	3.6
	Aeg5	6.30E−07	7.12E−07	1.002	273.9	16.5	1.000	71.1	72.2	0.998	181.9	6.5	1.13E−09	1.00	0.00	1.7
	Aeg6	6.25E−07	6.92E−07	1.008			0.997			0.995			3.57E−09	1.01	−0.69	1.1
	Aeg7	6.23E−07	7.31E−07	1.009			0.997			0.994			3.99E−09	1.01	−0.57	0.8
	Aeg8	6.15E−07	7.52E−07	1.008			1.001			0.991			4.11E−09	1.02	0.17	0.7
	Aeg9	6.08E−07	7.03E−07	1.011			0.997			0.992			4.92E−09	1.02	−0.52	0.8
	Aeg10	6.16E−07	7.18E−07	1.010	236.6	64.7	0.999	48.0	25.0	0.991	139.6	3.3	4.89E−09	1.02	−0.13	0.9
	Aeg11	5.68E−07	7.52E−07	1.019	75.2	60.2	1.000	236.1	28.4	0.981	330.6	8.3	8.72E−09	1.04	−0.03	0.6
Lithium pyroxenes																
Spodumene																
	NMB444	1.00E−08	1.81E−08	1.111	145.3	14.4	0.959	20.9	65.6	0.931	240.4	19.2	7.92E−10	1.19	−0.69	0.8
	Spod1	−8.29E−09	1.36E−10	1.059	359.0	9.2	1.013	90.0	6.2	0.927	213.3	78.9	4.54E−10	1.14	0.30	0.9
	Spod2	−7.51E−09	1.36E−10	1.059	211.4	13.5	1.020	302.2	3.3	0.922	45.7	76.1	4.33E−10	1.15	0.43	0.7
	Spod3	−6.85E−09	5.61E−09	1.112	79.1	6.6	0.963	183.6	65.3	0.925	346.2	23.7	5.50E−10	1.20	−0.59	0.9
	Spod4	−7.82E−09	5.61E−09	1.104	60.8	8.1	1.041	150.9	1.0	0.859	247.9	81.9	8.11E−10	1.18	−0.74	0.7
	fXl	−3.78E−08	5.44E−09	1.016	119.4	0.8	1.007	211.7	70.9	0.977	29.2	19.0	6.36E−10	1.04	0.56	0.9
	fXl2	−3.18E−08	5.48E−09	1.012	82.3	38.7	1.002	291.5	47.5	0.987	184.6	14.9	3.22E−10	1.03	0.18	0.6
							Orthopyroxenes									
Mg-Fe pyroxenes																
Enstatite																
	En1	1.22E−07	1.17E−07	1.055	0.6	88.8	0.986	186.7	1.2	0.959	96.7	0.1	4.95E−09	1.10	−0.44	11.6
	En2	7.74E−09	1.22E−08	1.082	160.5	86.2	0.974	24.2	2.8	0.944	294.1	2.6	4.59E−10	1.15	−0.57	1.8
	En3	7.00E−09	1.27E−08	1.095	37.0	87.9	0.981	188.5	1.9	0.924	278.6	1.0	4.97E−10	1.18	−0.33	2.3
	NMB45706	2.20E−07	1.83E−07	1.051	108.9	70.8	0.983	351.2	9.2	0.966	258.4	16.7	8.01E−09	1.09	−0.59	6.7
Hypersthene																
	Hyp1	1.08E−06	2.95E−07	1.407	357.7	4.6	0.923	127.9	82.9	0.670	267.2	5.4	3.29E−07	2.10	−0.31	127.6
	Hyp2	7.57E−07	2.95E−07	1.264	359.9	2.3	0.984	232.1	86.2	0.752	90.0	3.0	1.58E−07	1.68	−0.09	161.9

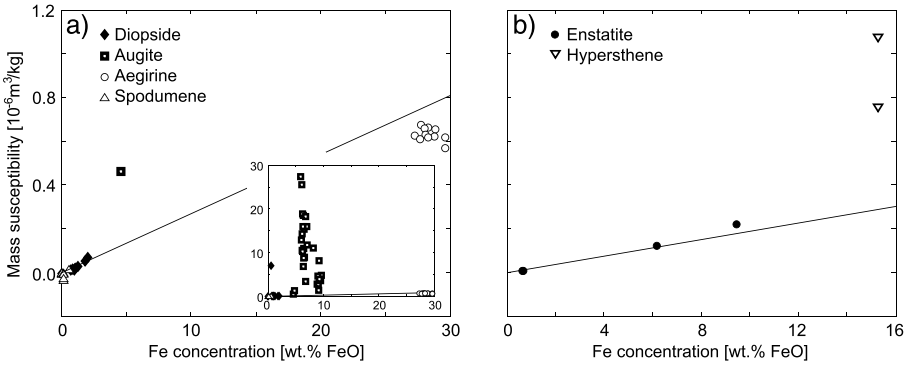

Figure 3. Mean mass susceptibility as a function of Fe concentration for (a) clinopyroxene, where the inset shows the large variation in susceptibility for some samples, particularly augite and (b) orthopyroxene. Solid lines represent theoretical susceptibility based on Fe concentration and assuming that Fe is present as Fe^{2+}.

remanent coercivities between 30 and 40 mT, which are still in the range expected for magnetite and maghemite. Their IRM is about 4 orders of magnitude lower than that of the augite and hypersthene samples. Saturation is reached below 1.0 T for most samples. However, the magnetization of En1 is approaching magnetic saturation up to 2.0 T, and Aeg3 is dominated by a high coercivity phase that is only approaching saturation above 1.4 T (Figure 4). In the samples with high IRM, the main remanence carrier reaches saturation below 1.0 T, which is a prerequisite for separation of ferromagnetic and paramagnetic contributions to the magnetic anisotropy.

3.4. Low-Field AMS

Principal directions of the low-field AMS are shown in Figure 5 for each mineral group. The low-field principal directions are consistent for diopside; k_2 is parallel to the crystallographic *b* axis, and k_1 and k_3 cluster at approximately ±45° from the *c* axis within the *a*-*c* plane. Augite shows a large variability in low-field principal directions. Part of the samples show a grouping of minimum susceptibility parallel to the crystallographic *b* axis. In aegirine, the maximum low-field susceptibility clusters close to the *c* axis, and the minimum is close to the crystallographic *a** axis. Principal directions in spodumene are variable. The maximum principal axis of enstatite groups around the crystallographic *c* axis. AMS shapes cover the whole range from prolate to oblate, especially for samples with weak anisotropy (Figure 6). Many augites have oblate AMS ellipsoids, whereas those of the orthopyroxenes are prolate (Table 3).

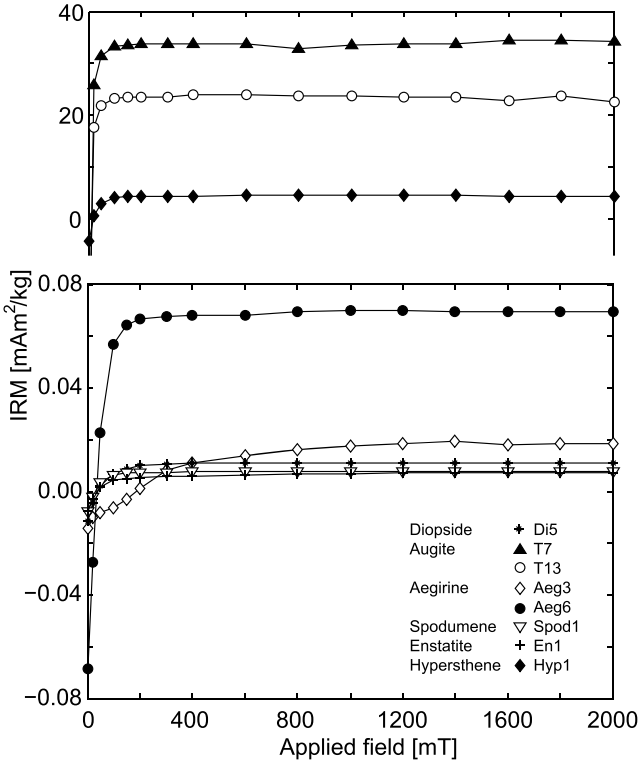

Figure 4. Isothermal remanent magnetization (IRM) acquisition curves for representative clinopyroxene and orthopyroxene samples.

3.5. Ferromagnetic AMS

One sample each of diopside and hypersthene and most augite crystals exhibit a significant ferromagnetic contribution to the high-field AMS. This ferromagnetic component was isolated, and directions of the ferromagnetic principal susceptibilities are plotted in

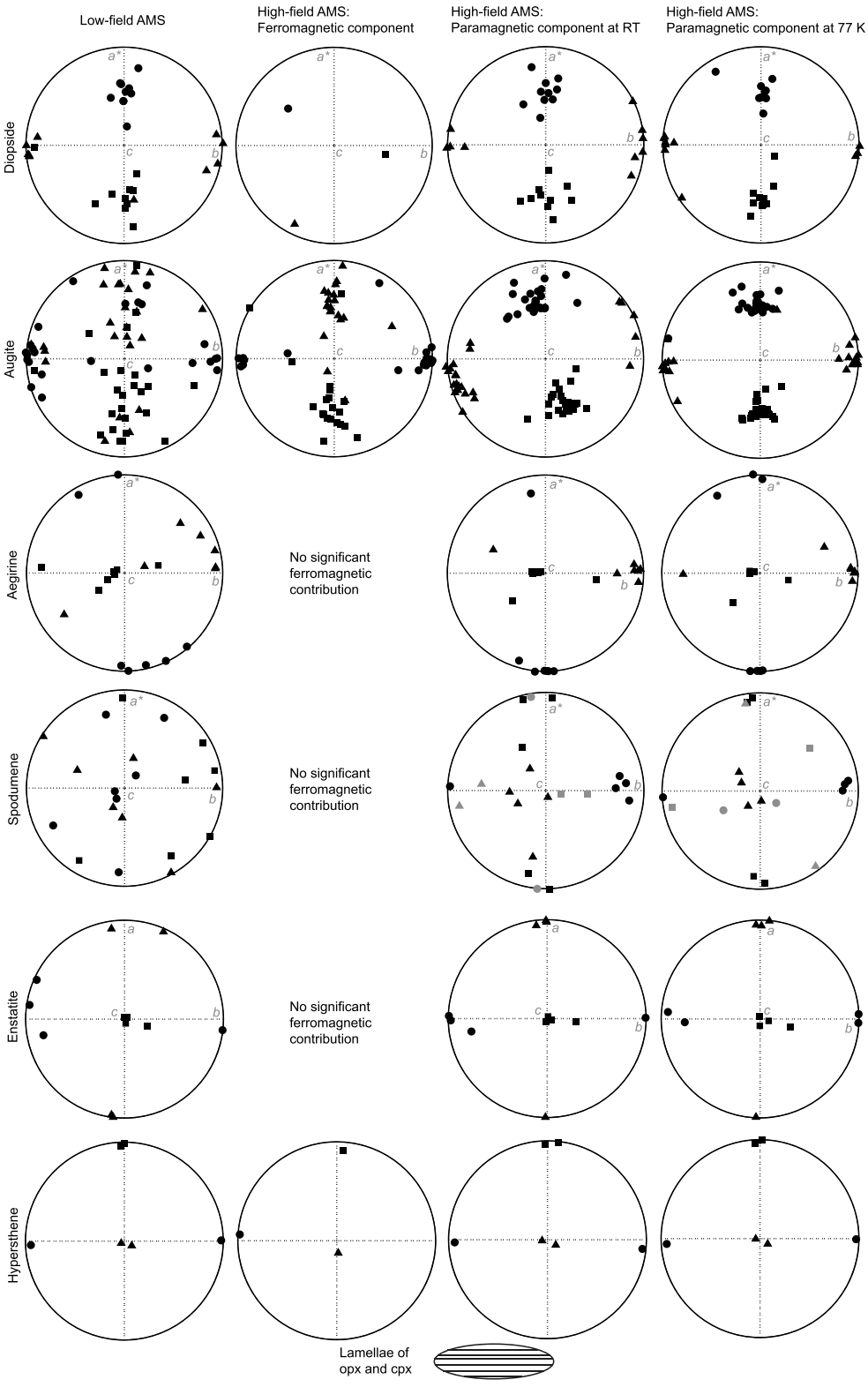

Figure 5. Equal area lower hemisphere stereoplots showing principal susceptibility directions for low-field AMS, ferromagnetic component of the high-field AMS at RT, and paramagnetic component of the high-field AMS at RT and 77 K for each mineral group. Directions are given in a crystallographic reference frame or relative to the orientation of the lamellae in hypersthene.

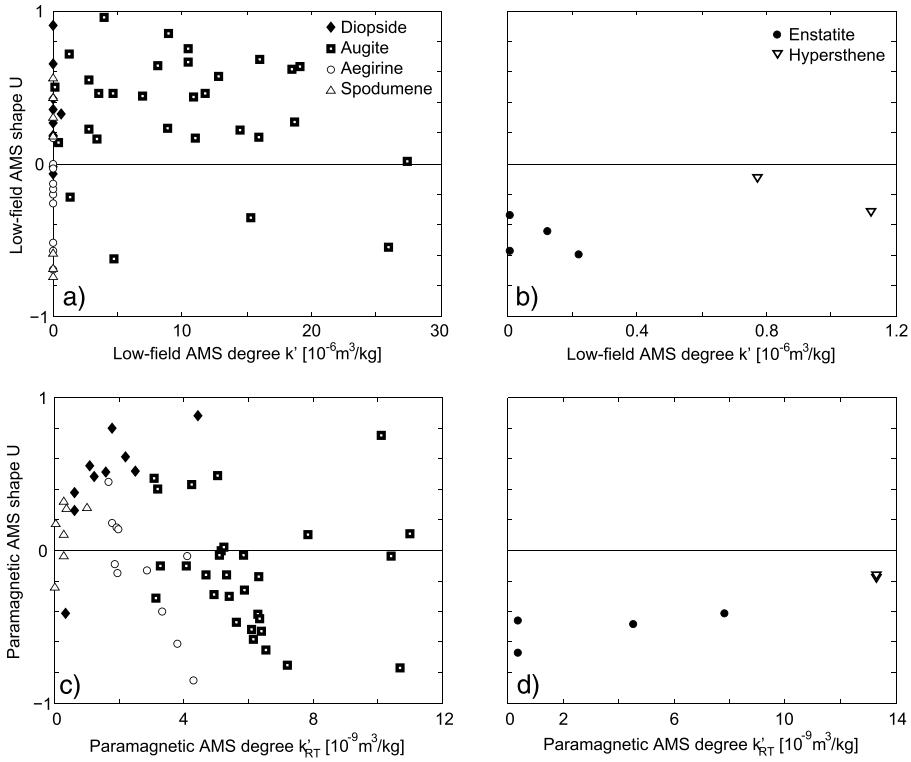

Figure 6. Modified Jelinek plot for (a, b) low-field AMS and (c, d) isolated paramagnetic AMS at RT. Data are plotted for (a, c) clinopyroxene and (b, d) orthopyroxene.

Figure 5. In most crystals, the minimum susceptibility of the ferromagnetic component is parallel to the crystallographic *b* axis of the clinopyroxene. The maximum and intermediate ferromagnetic susceptibilities lie in the *a*-*c* plane, at an approximately 45° angle to the crystallographic *c* axis. In hypersthene, the minimum and intermediate ferromagnetic susceptibilities lie in the plane of the exsolution lamellae and the maximum normal to this plane. With two exceptions, the shape of the ferromagnetic AMS is oblate. The ferromagnetic anisotropy degree *k*′ varies from 3.01×10^{-10} m^3/kg to 5.04×10^{-8} m^3/kg (Table 4).

3.6. Paramagnetic AMS

The paramagnetic component of the AMS was separated from the high-field AMS both at room temperature and at 77 K. Principal paramagnetic directions for each mineral group are shown in Figure 5, and the shape of the AMS ellipsoid and degree of anisotropy are show in Figure 6. Table 5 summarizes principal directions and AMS degree and shape parameters.

3.6.1. Clinopyroxene

For diopside and augite, the intermediate principal susceptibility is generally parallel to the crystallographic *b* axis, and k_1 and k_3 lie in the *a*-*c* plane, with k_1 approximately 45° inclined toward the $-a^*$ axis with respect to the *c* axis. The directions are better grouped at 77 K, where the paramagnetic signal is enhanced. Interestingly, the principal directions are rotated approximately 20° anticlockwise at room temperature with respect to the principal directions for augite at 77 K. Diopside AMS is oblate for all samples except Di2, which is diamagnetic. Augite generally displays a prolate AMS ellipsoid. The degree of deviatoric susceptibility *k*′ varies from 3.48×10^{-10} m^3/kg to 4.45×10^{-9} m^3/kg at room temperature in diopside and increases by a factor of 2.71 upon cooling to 77 K for Di2 and between 10.8 and 14.4 for the other diopside crystals. In augite, *k*′ is larger and ranges from 3.09×10^{-9} m^3/kg to 1.10×10^{-8} m^3/kg at room temperature. The increase in *k*′ when cooling to 77 K as defined by p_{77}′ is between 5.3 and 20.4, with the majority of samples showing p_{77}′ between 11 and 17.

The principal susceptibility axes are oriented differently in aegirine: k_1 is parallel to the crystallographic *c* axis, k_2 parallel to the *b* axis, and k_3 parallel to the a^* axis. The directions group well for the larger crystals (>4 g),

Journal of Geophysical Research: Solid Earth

10.1002/2014JB011678

Table 4. Principal Deviatoric Susceptibilities and Directions, AMS Degree, and Shape of the Ferromagnetic Component of the AMS at Room Temperature[a]

	Sample	Temperature	% Ferro	k_1 (m^3/kg)	D (deg)	I (deg)	k_2 (m^3/kg)	D (deg)	I (deg)	k_3 (m^3/kg)	D (deg)	I (deg)	U	dk (m^3/kg)	k' (m^3/kg)
							Clinopyroxenes								
Calcium pyroxenes															
Diopside															
	NMB15591	RT	28 ± 27	6.64E−10	100.0	45.4	2.82E−10	205.6	14.9	−9.46E−10	308.9	40.8	0.53	1.61E−09	6.87E−10
Augite															
	Aug1	RT	29 ± 3	3.21E−09	273.3	39.3	1.25E−09	85.3	50.4	−4.46E−09	180.1	3.9	0.49	7.67E−09	3.25E−09
	NMB42516	RT	33 ± 29	6.69E−09	192.0	55.2	9.45E−11	354.2	33.5	−6.79E−09	89.8	8.4	0.02	1.35E−08	5.50E−09
	NMB46281	RT	6 ± 3	3.75E−10	107.5	74.6	−1.41E−11	290.5	15.4	−3.61E−10	200.3	0.8	−0.06	7.36E−10	3.01E−10
	T1	RT	78 ± 8	1.54E−08	5.6	34.4	−4.92E−09	166.0	53.9	−1.05E−08	269.1	9.4	−0.57	2.59E−08	1.11E−08
	T3	RT	76 ± 60	1.26E−08	301.0	1.4	7.86E−10	204.3	78.3	−1.34E−08	31.3	11.7	0.09	2.60E−08	1.06E−08
	T4	RT	90 ± 41	3.65E−08	266.0	55.5	3.01E−08	5.7	6.6	−6.65E−08	100.1	33.7	0.88	1.03E−07	4.71E−08
	T6	RT	89 ± 49	2.72E−08	163.1	17.6	2.04E−08	61.2	32.9	−4.76E−08	276.6	51.6	0.82	7.48E−08	3.38E−08
	T7	RT	86 ± 4	4.18E−08	190.1	66.7	6.25E−09	1.1	23.1	−4.81E−08	92.5	3.3	0.21	8.99E−08	3.70E−08
	T8	RT	80 ± 13	1.97E−08	186.5	39.5	8.61E−09	356.2	50.1	−2.83E−08	92.3	5.1	0.54	4.80E−08	2.05E−08
	T9	RT	88 ± 4	4.51E−08	177.3	35.7	1.12E−08	5.8	54.0	−5.63E−08	270.2	4.1	0.33	1.01E−07	4.21E−08
	T10	RT	86 ± 7	3.86E−08	191.2	42.7	1.31E−08	352.7	45.8	−5.16E−08	92.4	9.4	0.43	9.02E−08	3.80E−08
	T12	RT	83 ± 43	2.34E−08	171.6	31.6	1.09E−08	7.8	57.4	−3.43E−08	266.2	7.3	0.57	5.77E−08	2.48E−08
	T13	RT	89 ± 7	5.05E−08	190.6	42.0	1.37E−08	356.4	47.1	−6.42E−08	94.2	7.1	0.36	1.15E−07	4.78E−08
	T14	RT	89 ± 30	5.15E−08	189.5	57.1	1.70E−08	350.8	31.5	−6.85E−08	86.1	8.5	0.43	1.20E−07	5.04E−08
	T15	RT	87 ± 10	3.62E−08	174.0	44.7	2.89E−09	352.7	45.3	−3.91E−08	83.4	0.6	0.12	7.53E−08	3.08E−08
	T16	RT	83 ± 9	2.81E−08	181.5	49.0	1.47E−08	0.7	41.0	−4.29E−08	91.0	0.4	0.62	7.10E−08	3.08E−08
	T17	RT	86 ± 6	2.85E−08	174.3	33.3	1.16E−08	13.7	55.2	−4.01E−08	270.4	9.1	0.51	6.86E−08	2.92E−08
	T18	RT	83 ± 21	2.96E−08	166.5	53.4	1.03E−08	359.9	35.9	−3.99E−08	265.2	6.4	0.44	6.95E−08	2.93E−08
	T19	RT	90 ± 24	4.68E−08	186.6	64.0	1.74E−08	1.2	25.9	−6.42E−08	92.2	2.1	0.47	1.11E−07	4.70E−08
	Vul1	RT	69 ± 55	6.63E−09	159.5	7.4	3.05E−09	321.7	82.2	−9.68E−09	69.2	2.4	0.56	1.63E−08	7.00E−09
	Vul5	RT	69 ± 52	1.10E−08			8.05E−09			−1.90E−08			0.80	3.00E−08	1.35E−08
	A4	RT	26 ± 7	1.84E−09	22.5	62.4	1.35E−09	26.0	26.0	−3.19E−09	213.1	8.7	0.81	5.03E−09	2.26E−09
	A6	RT	30 ± 20	1.38E−09	202.9	47.0	4.30E−10	39.6	39.6	−1.81E−09	50.4	14.0	0.40	3.19E−09	1.34E−09
							Orthopyroxenes								
Mg-Fe pyroxenes															
Hypersthene															
	Hyp1	RT	40 ± 18	1.03E−08	3.4	10.9	8.25E−10	176.8	79.0	−1.11E−08	273.1	1.2	0.11	2.14E−08	8.76E−09

[a]Data are shown when significant.

Journal of Geophysical Research: Solid Earth

10.1002/2014JB011678

Table 5. Principal Deviatoric Susceptibilities and Directions, AMS Degree, and Shape of the Paramagnetic Component of the AMS at Room Temperature and at 77 K

	Sample	Temperature	%para	k_1 (m^3/kg)	D (deg)	I (deg)	k_2 (m^3/kg)	D (deg)	I (deg)	k_3 (m^3/kg)	D (deg)	I (deg)	U	dk (m^3/kg)	p_{77}	k' (m^3/kg)	p_{77}'
								Clinopyroxenes									
Calcium pyroxenes																	
Diopside																	
	Di1	77 K	96 ± 39	5.14E−08	174.4	40.0	1.97E−08	267.1	3.2	−7.11E−08	0.9	49.8	0.48	1.23E−07		5.19E−08	
	Di1	RT	89 ± 26	3.44E−09	178.4	37.7	2.84E−09	268.4	0.0	−6.28E−09	358.4	52.3	0.88	9.72E−09	12.60	4.45E−09	11.67
	Di2	77 K	47 ± 205	1.25E−09	124.4	77.1	−2.34E−10	237.5	5.1	−1.02E−09	328.6	11.8	−0.31	2.27E−09		9.41E−10	
	Di2	RT	79 ± 292	4.71E−10	175.2	70.9	−1.12E−10	80.1	1.8	−3.58E−10	349.5	19.0	−0.41	8.29E−10	2.74	3.48E−10	2.71
	Di3	77 K	96 ± 79	1.33E−08	182.1	44.9	2.22E−09	273.2	1.1	−1.55E−08	4.3	45.1	0.23	2.88E−08		1.19E−08	
	Di3	RT	99 ± 8	1.05E−09	183.6	42.8	4.70E−10	273.9	0.3	−1.52E−09	4.3	47.2	0.55	2.57E−09	11.21	1.10E−09	10.78
	Di4	77 K	96 ± 73	3.25E−08	176.3	45.2	7.40E−09	270.3	3.9	−3.99E−08	4.1	44.5	0.31	7.24E−08		3.00E−08	
	Di4	RT	95 ± 69	2.43E−09	175.4	43.4	1.02E−09	269.0	3.9	−3.45E−09	3.1	46.3	0.52	5.88E−09	12.31	2.51E−09	11.98
	Di5	77 K	96 ± 47	1.96E−08	188.7	49.1	4.10E−09	94.0	4.0	−2.37E−08	0.5	40.6	0.28	4.33E−08		1.79E−08	
	Di5	RT	96 ± 79	1.55E−09	188.1	51.9	6.32E−10	93.4	3.7	−2.19E−09	0.5	37.8	0.51	3.74E−09	11.58	1.59E−09	11.26
	Di6	77 K	91 ± 113	1.47E−08	178.3	39.7	2.66E−09	88.1	0.3	−1.74E−08	357.8	50.3	0.25	3.21E−08		1.33E−08	
	Di6	RT	91 ± 58	1.22E−09	195.3	43.5	4.61E−10	95.2	10.4	−1.68E−09	354.8	44.6	0.48	2.90E−09	11.09	1.23E−09	10.80
	Di7	77 K	91 ± 181	8.67E−09	161.7	53.7	4.83E−10	271.2	13.8	−9.12E−09	10.3	32.8	0.08	1.78E−08		7.27E−09	
	Di7	RT	85 ± 62	6.96E−10	152.0	50.8	1.34E−10	268.1	19.8	−8.29E−10	11.3	32.3	0.26	1.52E−09	11.67	6.29E−10	11.55
	NMB15591	77 K	94 ± 65	2.67E−08	186.9	40.3	7.76E−09	95.7	1.5	−3.45E−08	4.0	49.6	0.38	6.12E−08		2.56E−08	
	NMB15591	RT	72 ± 32	1.45E−09	203.6	37.3	1.05E−09	108.4	6.8	−2.50E−09	9.7	51.9	0.80	3.95E−09	15.49	1.78E−09	14.41
	NMB346	77 K	87 ± 68	2.81E−08	178.5	39.2	6.29E−09	271.6	3.8	−3.44E−08	6.2	50.6	0.30	6.25E−08		2.59E−08	
	NMB346	RT	66 ± 71	2.02E−09	154.8	38.8	1.03E−09	63.4	1.7	−3.05E−09	331.2	51.1	0.61	5.07E−09	12.33	2.19E−09	11.80
	NMB5681	77 K	94 ± 35	8.06E−09	186.2	24.6	1.10E−09	276.4	1.0	−9.16E−09	10.1	65.4	0.19	1.72E−08		7.07E−09	
	NMB5681	RT	91 ± 19	6.43E−10	175.0	21.0	1.84E−10	84.5	2.9	−8.27E−10	339.9	68.6	0.38	1.47E−09	11.71	6.14E−10	11.52
Augite																	
	Aug1	77 K	94 ± 86	9.91E−08	276.8	55.5	2.99E−09	179.8	4.8	−1.02E−07	86.5	34.0	0.04	2.01E−07		8.21E−08	
	Aug1	RT	71 ± 8	9.27E−09	261.8	58.6	6.37E−10	353.0	0.7	−9.90E−09	83.4	31.4	0.10	1.92E−08	10.49	7.84E−09	10.48
	NMB42516	77 K	89 ± 70	1.41E−07	185.5	56.3	8.18E−09	91.2	2.9	−1.49E−07	359.3	33.5	0.08	2.90E−07		1.19E−07	
	NMB42516	RT	67 ± 25	1.29E−08	170.3	60.4	1.03E−09	264.5	2.4	−1.39E−08	355.8	29.5	0.11	2.68E−08	10.82	1.10E−08	10.81
	NMB46281	77 K	97 ± 60	6.62E−08	174.3	44.0	8.85E−09	266.6	2.3	−7.51E−08	358.9	45.9	0.19	1.41E−07		5.80E−08	
	NMB46281	RT	94 ± 5	4.98E−09	175.4	42.9	1.94E−09	265.6	0.2	−6.92E−09	355.8	47.1	0.49	1.19E−08	11.87	5.05E−09	11.49
	T1	77 K	66 ± 50	6.53E−08	173.7	44.5	−7.13E−10	264.0	0.4	−6.46E−08	354.4	45.5	−0.02	1.30E−07		5.30E−08	
	T1	RT	22 ± 5	4.18E−09	144.8	44.7	−7.79E−10	246.8	11.9	−3.40E−09	348.1	42.8	−0.31	7.58E−09	17.14	3.14E−09	16.87
	T2	77 K	79 ± 28	6.22E−08			4.47E−08			−1.07E−07			0.79	1.69E−07		7.60E−08	
	T2	RT	51 ± 28	8.54E−09			5.70E−09			−1.42E−08			0.75	2.27E−08	7.44	1.01E−08	7.51
	T3	77 K	76 ± 325	6.26E−08	181.0	44.4	2.66E−10	88.4	2.7	−6.29E−08	355.7	45.5	0.01	1.26E−07		5.12E−08	
	T3	RT	24 ± 28	4.14E−09	174.7	52.7	−2.61E−10	76.3	6.3	−3.88E−09	341.6	36.5	−0.10	8.02E−09	15.65	3.28E−09	15.62
	T4	77 K	48 ± 20	6.64E−08	188.8	40.8	−4.25E−09	92.6	7.2	−6.21E−08	354.4	48.3	−0.10	1.29E−07		5.25E−08	
	T4	RT	10 ± 14	7.17E−09	165.0	45.7	−1.31E−09	282.1	23.9	−5.86E−09	29.9	34.6	−0.30	1.30E−08	9.86	5.40E−09	9.73
	T5	77 K	37 ± 28	8.01E−08	184.6	49.2	−1.39E−08	90.8	3.3	−6.62E−08	358.0	40.6	−0.29	1.46E−07		6.05E−08	
	T5	RT	26 ± 179	6.33E−09	155.8	48.6	5.81E−12	254.3	7.4	−6.33E−09	350.7	40.4	0.00	1.27E−08	11.56	5.17E−09	11.71
	T6	77 K	56 ± 123	7.05E−08	174.6	45.9	−1.71E−09	266.6	1.9	−6.88E−08	358.5	44.1	−0.04	1.39E−07		5.69E−08	
	T6	RT	11 ± 16	4.32E−09	139.5	35.0	1.45E−09	245.0	21.0	−5.77E−09	359.7	47.5	0.43	1.01E−08	13.81	4.24E−09	13.40
	T7	77 K	24 ± 24	1.22E−07	182.8	48.8	−5.30E−08	80.1	10.8	−6.92E−08	341.2	39.2	−0.83	1.91E−07		8.66E−08	
	T7	RT	14 ± 3	7.26E−09	158.6	45.5	−1.56E−10	250.0	1.5	−7.10E−09	341.5	44.5	−0.03	1.44E−08	13.31	5.86E−09	14.76
	T8	77 K	44 ± 23	8.54E−08	184.0	42.4	−1.48E−08	92.4	1.8	−7.07E−08	0.5	47.6	−0.28	1.56E−07		6.46E−08	
	T8	RT	20 ± 13	6.37E−09	155.9	41.6	7.22E−11	251.0	5.7	−6.44E−09	347.2	47.9	0.02	1.28E−08	12.19	5.23E−09	12.35
	T9	77 K	27 ± 9	1.15E−07	171.1	43.8	−4.41E−08	265.0	4.1	−7.11E−08	359.2	46.0	−0.71	1.86E−07		8.21E−08	
	T9	RT	12 ± 2	7.73E−09	146.7	44.4	−1.22E−09	237.4	0.7	−6.51E−09	328.1	45.6	−0.26	1.−42E−08	13.07	5.88E−09	13.97
	T10	77 K	38 ± 21	1.14E−07	189.2	43.1	−4.26E−08	88.1	11.5	−7.15E−08	346.5	44.6	−0.69	1.86E−07		8.15E−08	

Journal of Geophysical Research: Solid Earth

10.1002/2014JB011678

Table 5. (continued)

	Sample	Temperature	%para	k_1 (m^3/kg)	D (deg)	I (deg)	k_2 (m^3/kg)	D (deg)	I (deg)	k_3 (m^3/kg)	D (deg)	I (deg)	U	dk (m^3/kg)	p_{77}	k' (m^3/kg)	p_{77}'
	T10	RT	14 ± 4	8.53E−09	148.9	47.0	−2.09E−09	53.6	4.9	−6.44E−09	319.1	42.5	−0.42	1.50E−08	12.39	6.29E−09	12.96
	T12	77 K	32 ± 15	9.33E−08	167.5	39.4	−2.57E−08	263.1	6.8	−6.−75E−08	1.3	49.8	−0.48	1.61E−07		6.81E−08	
	T12	RT	17 ± 45	6.31E−09	163.7	42.3	−1.24E−10	260.2	7.1	−6.18E−09	357.9	46.8	−0.03	1.25E−08	12.87	5.10E−09	13.36
	T13	77 K	27 ± 7	1.62E−07	188.7	44.2	−7.76E−08	18.4	45.4	−8.46E−08	283.4	4.9	−0.94	2.47E−07		1.15E−07	
	T13	RT	11 ± 3	7.68E−09	148.7	46.3	−2.07E−09	52.2	6.1	−5.61E−09	316.4	43.0	−0.47	1.33E−08	18.56	5.62E−09	20.40
	T14	77 K	34 ± 17	1.17E−07	198.5	38.3	−5.08E−08	89.0	22.9	−6.65E−08	335.8	43.0	−0.83	1.84E−07		8.30E−08	
	T14	RT	11 ± 15	8.83E−09	156.8	63.2	−2.64E−09	63.3	1.7	−6.18E−09	332.5	26.7	−0.53	1.50E−08	12.23	6.41E−09	12.96
	T15	77 K	30 ± 16	1.04E−07	171.7	48.4	−3.25E−08	264.1	2.1	−7.18E−08	356.0	41.5	−0.55	1.76E−07		7.53E−08	
	T15	RT	13 ± 4	6.04E−09	153.9	44.7	−6.29E−10	250.5	6.6	−5.41E−09	347.0	44.6	−0.16	1.15E−08	15.35	4.70E−09	16.04
	T16	77 K	34 ± 196	1.07E−07	177.9	50.2	−3.59E−08	86.9	0.8	−7.06E−08	356.3	39.8	−0.61	1.78E−07		7.69E−08	
	T16	RT	17 ± 8	8.13E−09	152.0	48.8	−8.78E−10	252.6	9.1	−7.25E−09	350.2	39.7	−0.17	1.54E−08	11.55	6.31E−09	12.18
	T17	77 K	32 ± 66	1.14E−07	187.8	44.5	−4.31E−08	97.8	0.0	−7.06E−08	7.7	45.5	−0.70	1.85E−07		8.13E−08	
	T17	RT	14 ± 3	6.54E−09	151.3	41.4	−1.16E−09	251.5	11.5	−5.38E−09	353.8	46.4	−0.29	1.19E−08	15.49	4.93E−09	16.48
	T18	77 K	38 ± 47	9.12E−08	171.3	44.2	−2.44E−08	269.1	8.0	−6.68E−08	7.1	44.7	−0.46	1.58E−07		6.68E−08	
	T18	RT	17 ± 11	8.52E−09	157.5	57.1	−2.76E−09	254.2	4.3	−5.77E−09	347.0	32.6	−0.58	1.43E−08	11.06	6.15E−09	10.86
	T19	77 K	28 ± 40	1.44E−07	170.1	65.8	−6.76E−08	76.5	1.6	−7.61E−08	345.8	24.1	−0.92	2.20E−07		1.02E−07	
	T19	RT	10 ± 17	6.83E−09	156.3	68.9	−7.11E−10	266.7	7.6	−6.12E−09	359.4	19.5	−0.16	1.30E−08	17.00	5.31E−09	19.17
	Vul1	77 K	55 ± 23	2.58E−08	141.5	62.5	9.84E−09	243.9	6.4	−3.56E−08	337.2	26.6	0.48	6.14E−08		2.60E−08	
	Vul1	RT	31 ± 35	3.31E−09	108.7	64.3	1.01E−09	240.8	17.9	−4.31E−09	336.8	17.8	0.40	7.62E−09	8.06	3.19E−09	8.15
	Vul2	77 K	53 ± 98	2.78E−08	232.7	55.7	1.60E−08	114.0	18.2	−4.38E−08	13.9	28.0	0.67	7.16E−08		3.13E−08	
	Vul2	RT	32 ± 77	5.17E−09	132.1	62.4	−3.35E−10	277.1	23.2	−4.84E−09	13.2	14.1	−0.10	1.00E−08	7.15	4.09E−09	7.66
	Vul3	77 K	70 ± 112	1.32E−07	176.1	48.3	2.94E−08	267.5	1.2	−1.61E−07	358.6	41.7	0.30	2.93E−07		1.21E−07	
	Vul3	RT	45 ± 312	1.29E−08	160.1	52.3	−3.86E−10	259.4	7.1	−1.26E−08	354.7	36.8	−0.04	2.55E−08	11.49	1.04E−08	11.66
	Vul4	77 K	56 ± 321	3.66E−08			1.71E−08			−5.37E−08			0.57	9.03E−08		3.88E−08	
	Vul4	RT	72 ± 60	1.01E−08			−4.05E−09			−6.06E−09			−0.75	1.62E−08	5.59	7.19E−09	5.40
	Vul5	77 K	55 ± 94	5.74E−08			−5.34E−09			−5.20E−08			−0.15	1.09E−07		4.48E−08	
	Vul5	RT	31 ± 50	8.40E−09			−2.49E−09			−5.91E−09			−0.52	1.43E−08	7.65	6.10E−09	7.35
	Vul6	77 K	54 ± 80	7.29E−08			−8.23E−09			−6.47E−08			−0.18	1.38E−07		5.65E−08	
	Vul6	RT	33 ± 130	1.50E−08			−6.16E−09			−8.89E−09			−0.77	2.39E−08	5.76	1.07E−08	5.29
	Vul7	77 K	40 ± 55	4.78E−08			−1.41E−08			−3.36E−08			−0.52	8.14E−08		3.47E−08	
	Vul7	RT	19 ± 47	9.11E−09			−3.24E−09			−5.87E−09			−0.65	1.50E−08	5.43	6.53E−09	5.31
	A4	77 K	83 ± 48	5.54E−08	277.1	7.3	−3.02E−09	173.6	61.3	−5.24E−08	10.9	27.6	−0.08	1.08E−07		4.41E−08	
	A4	RT	74 ± 10	8.65E−09	277.7	8.7	−2.24E−09	170.9	62.0	−6.41E−09	12.1	26.4	−0.45	1.51E−08	7.16	6.35E−09	6.94
	A6	77 K	85 ± 20	4.20E−08	196.7	38.0	5.15E−09	95.9	13.5	−4.72E−08	350.0	48.8	0.17	8.92E−08		3.66E−08	
	A6	RT	70 ± 27	3.07E−09	196.3	36.6	1.15E−09	94.7	15.1	−4.22E−09	346.4	49.5	0.47	7.29E−09	12.24	3.09E−09	11.86
Sodium pyroxenes																	
Aegirine																	
	Aeg1	77 K	88 ± 174	2.70E−08	282.7	84.4	−3.75E−09	94.9	5.6	−2.33E−08	185.0	0.7	−0.22	5.03E−08		2.07E−08	
	Aeg1	RT	96 ± 133	2.48E−09	275.8	85.1	−2.36E−10	95.5	4.9	−2.25E−09	185.5	0.0	−0.15	4.73E−09	10.63	1.94E−09	10.68
	Aeg2	77 K	95 ± 95	2.44E−08	289.5	86.4	−4.22E−10	89.0	3.4	−2.40E−08	179.1	1.3	−0.03	4.84E−08		1.98E−08	
	Aeg2	RT	95 ± 76	2.03E−09	286.1	86.8	2.60E−10	87.7	3.0	−2.29E−09	177.7	1.0	0.18	4.32E−09	11.20	1.77E−09	11.14
	Aeg3	77 K	94 ± 107	2.40E−08	276.0	86.8	1.15E−09	90.5	3.2	−2.51E−08	180.5	0.3	0.07	4.91E−08		2.01E−08	
	Aeg3	RT	96 ± 116	2.23E−09	276.6	85.3	2.34E−10	89.3	4.6	−2.47E−09	179.4	0.6	0.15	4.70E−09	10.45	1.93E−09	10.42
	Aeg4	77 K	91 ± 224	2.46E−08	265.5	82.3	4.77E−10	86.7	7.7	−2.51E−08	356.7	0.2	0.03	4.97E−08		2.03E−08	
	Aeg4	RT	94 ± 61	2.30E−09	268.0	80.2	2.33E−10	84.4	9.7	−2.53E−09	174.5	0.6	0.14	4.83E−09	10.29	1.98E−09	10.26
	Aeg5	77 K	93 ± 41	2.26E−08	282.7	82.4	−1.29E−09	87.5	7.3	−2.13E−08	177.8	2.0	−0.09	4.39E−08		1.79E−08	
	Aeg5	RT	96 ± 276	2.35E−09	275.6	80.0	−1.41E−10	88.3	9.9	−2.21E−09	178.5	1.2	−0.09	4.56E−09	9.63	1.86E−09	9.63
	Aeg6	77 K	91 ± 68	4.82E−08			−2.22E−08			−2.60E−08			−0.90	7.42E−08		3.41E−08	

Journal of Geophysical Research: Solid Earth

10.1002/2014JB011678

Table 5. (continued)

	Sample	Temperature	%para	k_1 (m^3/kg)	D (deg)	I (deg)	k_2 (m^3/kg)	D (deg)	I (deg)	k_3 (m^3/kg)	D (deg)	I (deg)	U	dk (m^3/kg)	p_{77}	k' (m^3/kg)	p_{77}'
	Aeg6	RT	75 ± 596	5.10E−09			−1.32E−10			−4.97E−09			−0.04	1.01E−08	7.37	4.11E−09	8.30
	Aeg7	77 K	79 ± 142	2.45E−08			−1.26E−09			−2.32E−08			−0.08	4.77E−08		1.95E−08	
	Aeg7	RT	70 ± 257	1.69E−09			5.90E−10			−2.28E−09			0.45	3.97E−09	12.02	1.67E−09	11.65
	Aeg8	77 K	78 ± 408	3.14E−08			−2.10E−09			−2.93E−08			−0.10	6.07E−08		2.48E−08	
	Aeg8	RT	92 ± 27	3.66E−09			−3.09E−10			−3.35E−09			−0.13	7.01E−09	8.66	2.87E−09	8.65
	Aeg9	77 K	85 ± 119	6.50E−08			−3.03E−08			−3.47E−08			−0.91	9.97E−08		4.60E−08	
	Aeg9	RT	73 ± 131	6.05E−09			−2.66E−09			−3.39E−09			−0.85	9.44E−09	10.56	4.29E−09	10.73
	Aeg10	77 K	77 ± 57	5.58E−08	223.6	56.7	−2.62E−08	67.4	31.0	−2.96E−08	330.8	10.9	−0.92	8.54E−08		3.95E−08	
	Aeg10	RT	78 ± 46	5.30E−09	230.9	54.2	−1.78E−09	90.2	29.2	−3.52E−09	349.2	18.8	−0.61	8.82E−09	9.68	3.81E−09	10.35
	Aeg11	77 K	71 ± 214	4.31E−08	100.7	65.3	−1.37E−08	270.2	24.3	−2.93E−08	2.0	4.0	−0.57	7.24E−08		3.11E−08	
	Aeg11	RT	50 ± 371	4.52E−09	95.7	46.3	−1.07E−09	295.8	41.9	−3.45E−09	196.5	10.2	−0.40	7.97E−09	9.08	3.34E−09	9.31
Lithium pyroxenes																	
Spodumene																	
	NMB444	77 K	56 ± 270	5.93E−09	355.9	7.8	1.60E−09	156.2	81.8	−7.53E−09	265.5	2.7	0.36	1.35E−08		5.61E−09	
	NMB444	RT	67 ± 163	1.11E−09	331.3	50.4	2.33E−10	188.7	33.3	−1.34E−09	85.7	18.9	0.28	2.45E−09	5.49	1.01E−09	5.54
	Spod1	77 K	40 ± 273	7.24E−10	258.6	12.3	−1.11E−10	351.4	12.9	−6.13E−10	126.5	72.0	−0.25	1.34E−09		5.51E−10	
	Spod1	RT	57 ± 75	3.48E−11	95.0	55.8	−5.06E−12	275.8	34.2	−2.97E−11	185.5	0.4	−0.24	6.45E−11	20.73	2.66E−11	20.75
	Spod2	77 K	29 ± 206	4.31E−10	49.4	33.4	7.42E−11	143.3	5.8	−5.05E−10	242.0	56.0	0.24	9.36E−10		3.86E−10	
	Spod2	RT	60 ± 106	3.63E−11	106.5	77.3	4.30E−12	259.3	11.3	−4.06E−11	350.5	5.6	0.17	7.69E−11	12.17	3.15E−11	12.23
	Spod3	77 K	74 ± 681	2.95E−09	351.7	11.9	−9.95E−11	215.9	73.6	−2.85E−09	84.0	11.1	−0.05	5.80E−09		2.37E−09	
	Spod3	RT	96 ± 73	3.75E−10	346.4	5.4	−1.10E−11	244.4	65.4	−3.64E−10	78.8	24.0	−0.04	7.39E−10	7.85	3.02E−10	7.85
	Spod4	77 K	63 ± 296	2.93E−09	184.3	15.1	−2.25E−10	312.7	66.5	−2.71E−09	89.4	17.6	−0.12	5.64E−09		2.31E−09	
	Spod4	RT	94 ± 53	3.59E−10	177.9	0.1	2.38E−11	268.1	60.0	−3.83E−10	87.9	30.0	0.10	7.42E−10	7.60	3.03E−10	7.61
	fXl	77 K	AMS not							significant							
	fXl	RT	89 ± 45	3.18E−10	3.7	4.9	7.59E−11	166.8	84.9	−3.94E−10	273.6	1.5	0.32	7.11E−10		2.95E−10	
	fXl2	77 K	72 ± 329	3.77E−09	177.2	7.4	−1.25E−10	292.1	73.0	−3.65E−09	85.2	15.3	−0.05	7.42E−09		3.03E−09	
	fXl2	RT	90 ± 25	4.19E−10	191.4	15.9	8.16E−11	325.3	67.6	−5.01E−10	96.9	15.3	0.27	9.20E−10	8.06	3.80E−10	7.97
							Orthopyroxenes										
Mg-Fe pyroxenes																	
Enstatite																	
	En1	77 K	88 ± 274	5.21E−08	332.5	88.0	−1.81E−08	182.6	1.7	−3.40E−08	92.6	1.0	−0.63	8.61E−08		3.74E−08	
	En1	RT	96 ± 57	6.22E−09	18.2	88.7	−1.71E−09	181.2	1.3	−4.51E−09	271.3	0.4	−0.48	1.07E−08	8.02	4.54E−09	8.23
	En2	77 K	83 ± 84	4.34E−09	182.8	84.0	−1.25E−09	357.5	6.0	−3.10E−09	87.5	0.6	−0.50	7.44E−09		3.16E−09	
	En2	RT	87 ± 37	5.12E−10	200.5	87.2	−1.86E−10	359.4	2.6	−3.26E−10	89.5	1.0	−0.67	8.38E−10	8.88	3.67E−10	8.63
	En3	77 K	81 ± 59	4.12E−09	104.7	83.5	−1.60E−09	4.3	1.2	−2.52E−09	274.2	6.4	−0.72	6.64E−09		2.94E−09	
	En3	RT	97 ± 14	5.06E−10	102.6	86.1	−1.34E−10	359.2	0.9	−3.72E−10	269.2	3.8	−0.46	8.78E−10	7.56	3.71E−10	7.92
	NMB45706	77 K	97 ± 56	8.91E−08	106.8	64.9	−2.79E−08	0.2	7.6	−6.13E−08	266.8	23.7	−0.56	1.50E−07		6.45E−08	
	NMB45706	RT	91 ± 16	1.06E−08	99.0	66.6	−2.55E−09	352.6	7.0	−8.07E−09	259.8	22.2	−0.41	1.87E−08	8.06	7.83E−09	8.23
Hypersthene																	
	Hyp1	77 K	89 ± 115	1.32E−07	356.7	5.6	−3.58E−08	132.8	82.3	−9.65E−08	266.2	5.3	−0.47	2.29E−07		9.66E−08	
	Hyp1	RT	60 ± 14	1.72E−08	358.4	5.3	−1.93E−09	130.0	82.1	−1.52E−08	267.8	5.9	−0.18	3.24E−08	7.05	1.33E−08	7.27
	Hyp2	77 K	91 ± 117	1.33E−07	0.8	1.1	−3.59E−08	255.6	85.7	−9.73E−08	90.9	4.1	−0.47	2.30E−07		9.74E−08	
	Hyp2	RT	67 ± 154	1.71E−08	6.0	2.1	−1.71E−09	253.0	84.7	−1.54E−08	96.1	4.9	−0.16	3.25E−08	7.09	1.33E−08	7.31

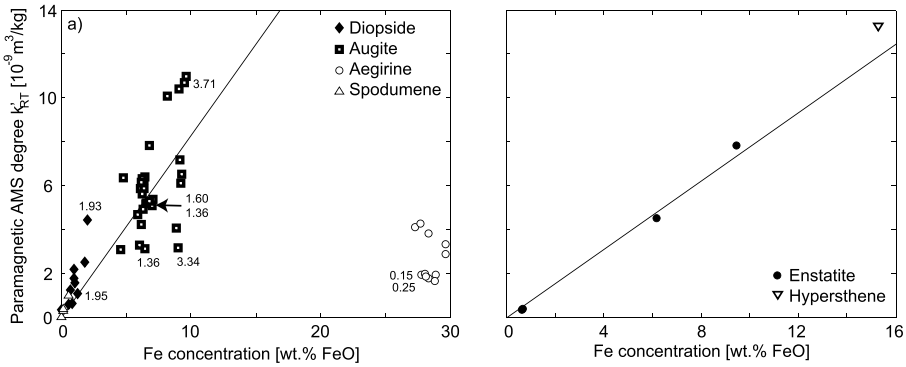

Figure 7. Anisotropy degree (k') as a function of Fe concentration for (a) clinopyroxene, in which Fe^{2+}/Fe^{3+} ratios are shown where available, and (b) orthopyroxene.

whereas those of the smaller samples (<0.5 g) are more scattered. AMS shapes cover a wide range from prolate to oblate, and k' varies from 1.67×10^{-9} m^3/kg to 4.29×10^{-9} m^3/kg. The deviatoric susceptibility is 8.30–11.65 times larger at 77 K.

Two types of behavior can be seen in spodumene; the Fe-richer varieties have the minimum susceptibility parallel to the *b* axis, whereas the Fe-poor ones have k_3 parallel to a^* at RT but close to *c* at 77 K. AMS shapes vary considerably for individual samples, which is attributed to their weak susceptibility. The anisotropy degree k' ranges from 2.66×10^{-11} m^3/kg to 1.01×10^{-9} m^3/kg at room temperature and increases 5.54 to 20.75 times when measured at 77 K. The large increase in Spod1 and Spod2 relates to the contribution of a diamagnetic component at RT.

The degree of the paramagnetic AMS k' shows a general increase with Fe concentration for spodumene, diopside, and augite (Figure 7). Therefore, k' can be estimated from the Fe concentration by

$$k' = 8.28 \times 10^{-10} \times Fe \text{ m}^3/\text{kg}$$

where *Fe* is the Fe concentration in wt % FeO. Aegirine possesses a lower degree of anisotropy than predicted by this trend, which is discussed below.

3.6.2. Orthopyroxene

Enstatite has its maximum principal susceptibility parallel to *c*, the intermediate susceptibility parallel to the *a* axis and minimum parallel to the *b* axis, both at room temperature and at 77 K. The AMS ellipsoid has a prolate shape, and k' varies between 3.67×10^{-10} m^3/kg and 7.83×10^{-9} m^3/kg. The anisotropy increases by a factor of 7.27–8.63 when the measurement temperature is 77 K compared to room temperature.

The maximum susceptibility of hypersthene, which consists of lamellae of orthopyroxene and Ca-rich clinopyroxene, is normal to these exsolution lamellae, whereas k_2 and k_3 lie in the plane of the lamellae. For hypersthene, the AMS has a less prolate shape than for enstatite, probably due to a superposition of the orthopyroxene and clinopyroxene anisotropies. p_{77}' varies between 7.27 and 7.31.

Similar to the clinopyroxene crystals, k' of enstatite increases with Fe concentration (Figure 7b):

$$k' = 7.80 \times 10^{-10} \times Fe \text{ m}^3/\text{kg}.$$

Hypersthene has a slightly higher AMS degree than expected from the enstatite trend and its Fe concentration. This may be explained by the superposition of clinopyroxene and orthopyroxene anisotropy, as k' is larger for clinopyroxene than orthopyroxene for a given Fe content.

4. Discussion

4.1. Mass Susceptibility and Chemical Composition

Vernon [1961] proposed that magnetic susceptibility can be used as a measure of Fe and Mn contents in silicates. A good correlation is observed between Fe concentration and susceptibility in diopside, aegirine, and enstatite (Figure 3). In augite and hypersthene, however, the susceptibility appears to be mainly controlled by the amount of ferromagnetic inclusions, such as magnetite, within the crystals. This effect is

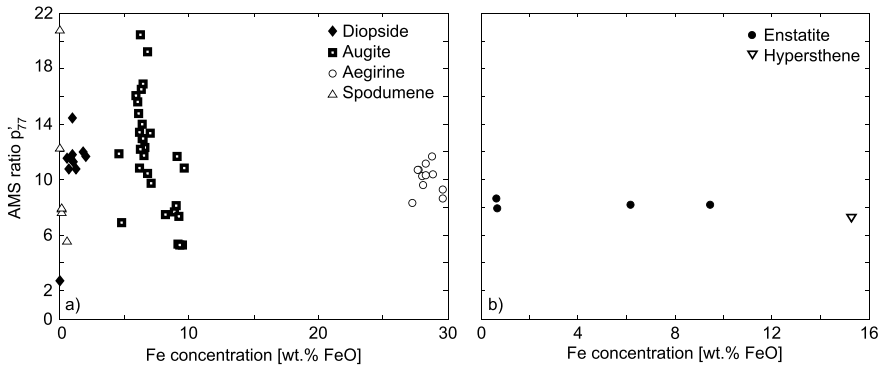

Figure 8. Factor p_{77}' as a function of Fe concentration for the different mineral groups: (a) clinopyroxene and (b) orthopyroxene.

larger than the dependence on Fe concentration in the structure and illustrates the importance of knowing which mineral carries the magnetic susceptibility. In the absence of ferromagnetic inclusions within clinopyroxene or orthopyroxene, the mass susceptibility shows a good linear correlation with Fe concentration.

4.2. Paramagnetic Anisotropy Degree and Its Dependence on Fe Concentration

The degree of anisotropy, k', increases with Fe concentration in both clinopyroxene, with the exception of aegirine, and orthopyroxene. There is a larger variation in this relationship in clinopyroxene (Figure 7), whereas it is more linear in enstatite. Aegirine has a small anisotropy degree given its large Fe content. Mössbauer spectroscopy revealed that aegirine mainly contains Fe^{3+}, whereas Fe^{2+} dominates in the diopside-augite series. It has been argued that Fe^{2+} possesses a strong ionic magnetic anisotropy in the trigonal crystal field in micas, whereas Fe^{3+} is isotropic [*Ballet and Coey*, 1982; *Beausoleil et al*., 1983]. Because the M1 sites in clinopyroxene are similar to the M2 sites in biotite in terms of the crystal field to which the cation is subjected [*Burns*, 1993], a similar argument could hold for aegirine. Therefore, if the Fe^{3+} in aegirine is isotropic, only Fe^{2+} would cause an anisotropy. The presence of Fe^{3+}, hence variable Fe^{2+}/Fe^{3+}, may also explain some of the scatter in k' found in the diopside and augite crystals that have similar total Fe concentration. Orthopyroxene rarely incorporates Fe^{3+} and thus shows a better constrained linear relationship between AMS degree and Fe concentration.

The degree of anisotropy increases by varying amounts at 77 K, with an increase between 3 and 21 in the diopside-augite series, 8 and 12 for aegirine, and 5 and 21 for spodumene. No clear dependence is found between p_{77}' and Fe concentration in clinopyroxenes (Figure 8). The diopside Di2 and spodumene NMB444 show low p_{77}' values of 2.71 and 5.54, respectively. The spodumene crystals Spod1 and Spod2 display large p_{77}' between 12.23 and 20.75. Together with the negative or weak positive mean susceptibilities, this suggests a contribution of a temperature-independent diamagnetic AMS in these crystals. Interestingly, p_{77}' is close to 8 in all orthopyroxenes, a value that is similar to p_{77} found in siderite [*Schmidt et al*., 2007a], the sheet silicate minerals muscovite, phlogopite and chlorite [*Biedermann et al*., 2014a], olivine [*Biedermann et al*., 2014b], and some members of the amphibole group [*Biedermann*, 2014].

4.3. Paramagnetic Principal Directions and Crystal Structure

In clinopyroxene, which possesses monoclinic symmetry, one of the principal susceptibility directions has to be parallel to the crystallographic *b* axis, whereas there are no constraints on the other two principal susceptibility directions. These constraints are imposed by crystal symmetry [*Neumann*, 1885; *Nye*, 1957]. The paramagnetic k_2 axes are parallel to the *b* axis in diopside, and the minimum and maximum susceptibilities lie in the *a*-*c* plane. The principal axes of the AMS ellipsoid of augite show a similar orientation at 77 K, but the susceptibility tensor is rotated at room temperature; k_2 is rotated up to 40° away from *b*. Crystal symmetry does not allow this rotation, which occurs only in those samples with significant ferromagnetic contributions. Therefore, we suggest that the rotation represents an artifact related to the ferromagnetic inclusions, i.e., that the magnetic field is disturbed locally by their strong magnetization. The principal directions determined in this study agree with the orientation of the k_2 axis proposed by *Parry* [1971] and *Lagroix and Borradaile* [2000],

but not with the orientation of k_1 described by *Finke* [1909]. In addition, the results presented here show that not only k_2 but also k_1 and k_3 have clearly defined orientations with respect to the crystal lattice.

In aegirine, all three principal paramagnetic susceptibilities are parallel to one crystallographic axis, and thus, the symmetry of the susceptibility tensor is higher than required by crystal symmetry. The difference in orientation of the principal axes compared to the diopside-augite series may be explained by the different predominant oxidation state of Fe or by small changes in the unit cell imposed by the different sizes and charge of Ca and Na cations on the M2 site.

Interestingly, the different orientation of the susceptibility tensor with respect to crystal lattice in aegirine as opposed to the diopside-augite series is in agreement with the orientation of the optical indicatrix in these minerals. In aegirine, the principal axes of the indicatrix are inclined 0–10° with respect to the *c* and *a** crystallographic axes, and in diopside-augite the inclination varies between 35° and 48° [*Tröger*, 1982]. Even though maximum and minimum susceptibility do not always coincide with the same indicatrix axes, this confirms the crystallographic control of the magnetic anisotropy. More work would be needed, however, in order to understand why k_1 is oriented at a 45° angle from the crystallographic *c* axis in diopside and augite.

The magnetic anisotropy in spodumene is a superposition of a diamagnetic and a paramagnetic component. Principal directions are consistent for samples with similar Fe concentrations, i.e., for Spod1 and Spod2 with 0.005 wt % FeO or for the group with 0.2–0.6 wt % FeO consisting of Spod3, Spod4, NMB444, fXl and fXl2, but differ between the groups. Because Spod1 and Spod2 have the lowest Fe concentration, their anisotropy ellipsoids may represent the diamagnetic fraction of the susceptibility.

For orthopyroxene, the principal directions of any second-order tensor property are each parallel to one of the crystallographic axes, as required by the orthorhombic symmetry. Enstatite has its maximum susceptibility aligned with the crystallographic *c* axis, and k_2 and k_3 are parallel to the *a* and *b* axes, respectively. One sample deviates from this general behavior, which is due to a small misorientation of the crystal. *Lagroix and Borradaile* [2000] have already proposed the alignment of k_1 parallel to *c*. However, they did not find any relation between k_2 and k_3 with the *a* or *b* axes, violating crystal symmetry constraints. They explained this by the effects of ferromagnetic inclusions or misorientation. Isolating the paramagnetic anisotropy demonstrates that k_3 is parallel to the crystallographic *b* axis in enstatite. These results seemingly contradict findings by *Wiedenmann et al*. [1986], who measured Fe-rich orthopyroxenes and found that the maximum susceptibility is parallel to *b*. Their samples differ considerably from this collection, however, because they have a significantly larger Fe concentration and both M1 and M2 sites are occupied predominantly by Fe. Crystals used in this study have low Fe concentrations and the Fe is located mainly in M2 sites.

4.4. Ferromagnetic Inclusions

Many pyroxenes, especially augite, contain ferromagnetic inclusions, which, even when their abundances are small, clearly dominate the magnetic susceptibility and its anisotropy in low fields. There are two principal types of occurrence of magnetite in augite: (1) accidental magnetite inclusions (incorporated in augite during crystal growth) and (2) magnetite forming as exsolution products upon cooling of augite crystals, where the magnetite (111) plane often lies parallel to (100) of the augite and (−110) parallel to (010). If there are needles of magnetite, these lie in the (010) plane and are elongated parallel or perpendicular to [001] [*Bown and Gay*, 1959; *Deer et al*., 1978; *Feinberg et al*., 2004, 2006]. The consistency of ferromagnetic principal susceptibility directions exhibited by the samples thus suggests that magnetite inclusion of type (2) predominates.

If clinopyroxene is preferentially oriented in a rock, and type (2) magnetite inclusions within this pyroxene carry a remanent magnetization, the recorded paleomagnetic direction could be deflected away from the direction of the magnetizing field. Furthermore, paleointensity studies made on single-pyroxene crystals may yield inconsistent results when an isotropic susceptibility is assumed. Thus, paleomagnetic studies in rocks with a strong mineral fabric need to consider this aspect when interpreting paleomagnetic data.

5. Conclusions

The paramagnetic anisotropy in clinopyroxenes and orthopyroxenes is clearly related to the crystal lattice of each mineral group and to the concentration, dominant site distribution and oxidation state of Fe in each mineral. In clinopyroxene, the Fe atoms are located mainly in M1 sites and the directions of the principal

susceptibilities are k_2 // b and k_1, k_3 in the a-c plane in the diopside-augite series, and k_1 // c, k_2 // b, and k_3 // a^* in aegirine. There is a general trend of increasing AMS degree with increasing Fe concentration. The AMS degree is, however, affected by the Fe^{2+}/Fe^{3+} ratio, which results in a low AMS degree for aegirine, due to its large Fe^{3+} concentration. In enstatite, the maximum susceptibility is parallel to the crystallographic c axis, and the intermediate and minimum susceptibilities are aligned with a and b axes, respectively. The AMS degree increases nearly linearly with Fe concentration. These results can be used together with orientation distribution functions of the respective minerals in order to model paramagnetic anisotropy in a pyroxene-bearing rock. Further, they will help in interpreting AMS, e.g., in ultramafic and mafic rocks in terms of crystallographic preferred orientation of the pyroxenes.

This study demonstrates that ferromagnetic inclusions are present mainly in augite and that preferred orientation of these inclusions causes a strong ferromagnetic anisotropy. This may dominate the low-field anisotropy and mask the anisotropy originating from the paramagnetic pyroxene. Therefore, if AMS is used as a proxy for pyroxene texture, it is necessary to isolate the paramagnetic contribution to the total magnetic anisotropy. The confinement of magnetite within the pyroxene lattice also should be considered in paleomagnetic studies employing rock samples with oriented pyroxene crystals.

Acknowledgments

A. Puschnig (Natural History Museum Basel), A. Stucki (Siber + Siber Aathal), and P. Brack and S. Bosshard (ETH Zurich) kindly provided samples for this study. We are grateful to D. Logvinovich (Laboratory of Crystallography, ETH Zurich) for an introduction to Laue orientation and assistance during measurements. We thank P.A. Selkin and F. Lagroix for their careful reviews of the manuscript. This project was funded by the Swiss National Science Foundation, project 200020_143438.

References

Abdu, Y. A., and F. C. Hawthorne (2013), Local structure in *C*2/*c* clinopyroxenes on the hedenbergite ($CaFeSi_2O_6$)-ferrosilite ($Fe_2Si_2O_6$) join: A new interpretation for the Mössbauer spectra of Ca-rich C2/*c* clinopyroxenes and implications for pyroxene exsolution, *Am. Mineral.*, *98*, 1227–1234, doi:10.2138/am.2013.4328.

Almqvist, B. S. G., M. Herwegh, V. Schmidt, T. Pettke, and A. M. Hirt (2010), Magnetic susceptibility as a tool to study deformed calcite with variable impurity content, *Geochem. Geophys. Geosyst.*, *11*, Q01Z09, doi:10.1029/2009GC002900.

Archanjo, C. J., and J. L. Bouchez (1997), Magnetic fabrics and microstructures of the post-collisional aegirine-augite syenite Triunfo pluton, northeast Brazil, *J. Struct. Geol.*, *19*(6), 849–860, doi:10.1016/S0191-8141(97)00008-4.

Ballet, O., and J. M. D. Coey (1982), Magnetic properties of sheet silicates: 2:1 layer minerals, *Phys. Chem. Miner.*, *8*, 218–229, doi:10.1007/BF00309481.

Beausoleil, N., P. Lavallee, A. Yelon, O. Ballet, and J. M. D. Coey (1983), Magnetic properties of biotite micas, *J. Appl. Phys.*, *54*(2), 906–915, doi:10.1063/1.332053.

Bergmüller, F., C. Bärlocher, B. Geyer, M. Grieder, F. Heller, and P. Zweifel (1994), A torque magnetometer for measurements of the high-field anisotropy of rocks and crystals, *Meas. Sci. Technol.*, *5*(12), 1466–1470, doi:10.1088/0957-0233/5/12/007.

Biedermann, A. R. (2014), Magnetic anisotropy of common rock-forming minerals, PhD thesis Nr 21989, ETH Zurich, Zurich, doi:10.3929/ethz-a-010252738.

Biedermann, A. R., W. Lowrie, and A. M. Hirt (2013), A method for improving the measurement of low-field magnetic susceptibility anisotropy in weak samples, *J. Appl. Geophys.*, *88*, 122–130, doi:10.1016/j.jappgeo.2012.10.008.

Biedermann, A. R., C. Bender Koch, W. E. A. Lorenz, and A. M. Hirt (2014a), Low-temperature magnetic anisotropy in micas and chlorite, *Tectonophysics*, *629*, 63–74, doi:10.1016/j.tecto.2014.01.015.

Biedermann, A. R., T. Pettke, E. Reusser, and A. M. Hirt (2014b), Anisotropy of magnetic susceptibility in natural olivine single crystals, *Geochem. Geophys. Geosyst.*, *15*, 3051–3065, doi:10.1002/2014GC005386.

Bleil, U., and N. Petersen (1982), Magnetische eigenschaften der minerale, in *Landolt-Börnstein—Numerical Data and Functional Relationships in Science and Technology-Group V: Geophysics and Space Research*, edited by G. Angenheister, pp. 312–320, Springer, Berlin.

Borradaile, G. J., and B. Henry (1997), Tectonic applications of magnetic susceptibility and its anisotropy, *Earth Sci. Rev.*, *42*, 49–93, doi:10.1016/S0012-8252(96)00044-X.

Bown, M. G., and P. Gay (1959), The identification of oriented inclusions in pyroxene crystals, *Am. Mineral.*, *44*, 592–602.

Burns, R. G. (1993), *Mineralogical Applications of Crystal Field Theory*, 2nd ed., Cambridge Univ. Press, Cambridge, U. K.

Deer, W. A., R. A. Howie, and J. Zussman (1978), *Single-Chain Silicates*, 668 pp., Longman Group Ltd, London, U. K.

Feinberg, J. M., H.-R. Wenk, P. R. Renne, and G. R. Scott (2004), Epitaxial relationships of clinopyroxene-hosted magnetite determined using electron backscatter diffraction (EBSD) technique, *Am. Mineral.*, *89*, 462–466.

Feinberg, J. M., R. J. Harrison, T. Kasama, R. E. Dunin-Borkowski, G. R. Scott, and P. R. Renne (2006), Effects of internal mineral structures on the magnetic remanence of silicate-hosted titanomagnetite inclusions: An electron holography study, *J. Geophys. Res.*, *111*, B12S15, doi:10.1029/2006JB004498.

Finke, W. (1909), Magnetische messungen an platinmetallen und monoklinen kristallen, insbesondere der eisen-, kobalt- und nickelsalze, *Ann. Phys.*, *336*(1), 149–168, doi:10.1002/andp.19093360108.

Guillong, M., D. L. Meier, M. M. Allan, C. A. Heinrich, and B. W. D. Yardley (2008), SILLS: A MATLAB-based program for the reduction of laser ablation ICP-MS data of homogeneous materials and inclusions, *Miner. Assoc. Can. Short Course*, *40*, 328–333.

Hrouda, F. (1982), Magnetic anisotropy of rocks and its application in geology and geophysics, *Geophys. Surv.*, *5*, 37–82, doi:10.1007/BF01450244.

Jelinek, V. (1981), Characterization of the magnetic fabric of rocks, *Tectonophysics*, *79*, T63–T67, doi:10.1016/0040-1951(81)90110-4.

Jelinek, V. (1984), On a mixed quadratic invariant of the magnetic susceptibility tensor, *J. Geophys. Res.*, *56*(1), 58–60.

Lagroix, F., and G. J. Borradaile (2000), Magnetic fabric interpretation complicated by inclusions in mafic silicates, *Tectonophysics*, *325*, 207–225, doi:10.1016/S0040-1951(00)00125-6.

Laugier, J., and A. Filhol (1983), An interactive program for the interpretation and simulation of Laue patterns, *J. Appl. Crystallogr.*, *16*, 281–283, doi:10.1107/S0021889883010420.

Martín-Hernández, F., and A. M. Hirt (2001), Separation of ferrimagnetic and paramagnetic anisotropies using a high-field torsion magnetometer, *Tectonophysics*, *337*(3–4), 209–221, doi:10.1016/S0040-1951(01)00116-0.

Neumann, F. E. (Ed.) (1885), *Vorlesungen über die Theorie der Elastizität der Festen Körper und des Lichtäthers*, B.G. Teubner Verlag, Leipzig, Germany.

Nye, J. F. (1957), *Physical Properties of Crystals: Their Representation by Tensors and Matrices*, 322 pp., Clarendon Press, Oxford, U. K.
Parks, G. A., and S. Akhtar (1968), Magnetic moment of Fe^{2+} in paramagnetic minerals, *Am. Mineral.*, *53*, 406–415.
Parry, G. R. (1971), The magnetic anisotropy of some deformed rocks, PhD thesis, 218 pp., Univ. of Birmingham, Birmingham, U. K.
Pettke, T., F. Oberli, A. Audetat, M. Guillong, A. Simon, J. Hanley, and L. M. Klemm (2012), Recent developments in element concentration and isotope ratio analysis of individual fluid inclusions by laser ablation single and multiple collector ICP-MS, *Ore Geol. Rev.*, *44*, 10–38, doi:10.1016/j.oregeorev.2011.11.001.
Redhammer, G. J., G. Amthauer, G. Roth, G. Tippelt, and W. Lottermoser (2006), Single-crystal X-ray diffraction and temperature dependent ^{57}Fe Mössbauer spectroscopy on the hedenbergite-aegirine (Ca,Na)(Fe^{2+},Fe^{3+})Si_2O_6 solid solution, *Am. Mineral.*, *91*, 1271–1292, doi:10.2138/am.2006.2173.
Schmidt, V., A. M. Hirt, K. Hametner, and D. Gunther (2007a), Magnetic anisotropy of carbonate minerals at room temperature and 77 K, *Am. Mineral.*, *92*(10), 1673–1684, doi:10.2138/am.2007.2569.
Schmidt, V., A. M. Hirt, P. Rosselli, and F. Martín-Hernández (2007b), Separation of diamagnetic and paramagnetic anisotropy by high-field, low-temperature torque measurements, *Geophys. J. Int.*, *168*(1), 40–47, doi:10.1111/j.1365-246X.2006.03202.x.
Selkin, P. A., S. J. Gee, and W. P. Meurer (2014), Magnetic anisotropy as a tracer of crystal accumulation and transport, Middle Banded Series, Stillwater Complex, Montana, *Tectonophysics*, *629*, 123–137, doi:10.1016/j.tecto.2014.03.028.
Spandler, C., T. Pettke, and D. Rubatto (2011), Internal and external fluid sources for eclogite-facies veins in the Monviso meta-ophiolite, Western Alps: Implications for fluid flow in subduction zones, *J. Petrol.*, *52*, 1207–1236.
Tröger, W. E. (1982), *Optische Bestimmung der Gesteinsbildenden Minerale*, *Teil 1 Bestimmungstabellen*, 5 Auflage ed., E. Schweizerbart'sche Verlagsbuchhandlung, Stuttgart, Germany.
Vernon, R. H. (1961), Magnetic susceptibility as a measure of total iron plus manganese in some ferromagnesian silicate minerals, *Am. Mineral.*, *46*, 1141–1153.
Wagner, J.-J., I. G. Hedley, D. Steen, C. Tinkler, and M. Vuagnat (1981), Magnetic anisotropy and fabric of some progressively deformed ophiolitic gabbros, *J. Geophys. Res.*, *86*(B1), 307–315, doi:10.1029/JB086iB01p00307.
Werbel, B., V. H. Dibeler, and W. C. Vosburgh (1943), Complex ions: VI. The magnetic moments of some iron(III) complex ions, *J. Am. Chem. Soc.*, *65*(12), 2329–2334, doi:10.1021/ja01252a022.
Wiedenmann, A., J.-R. Regnard, G. Fillion, and S. S. Hafner (1986), Magnetic properties and magnetic ordering of the orthopyroxenes $Fe_xMg_{1-x}SiO_3$, *J. Phys. C: Solid State Phys.*, *19*(19), 3683–3695, doi:10.1088/0022-3719/19/19/022.